

Linear and conservative IMEX Runge–Kutta finite difference schemes with provable energy stability for the Cahn–Hilliard model in arbitrary domains

Junseok Kim^a, Zhijun Tan^{b,c}, Junxiang Yang^{b,*}

^a Department of Mathematics, Korea University, Seoul, 02841, Republic of Korea

^b School of Computer Science and Engineering, Sun Yat-sen University, Guangzhou 510006, China

^c Guangdong Province Key Laboratory of Computational Science, Sun Yat-sen University, Guangzhou 510275, China



ARTICLE INFO

Keywords:

Cahn–Hilliard equation
Finite difference method
Energy stable schemes
Arbitrary domains

ABSTRACT

The Cahn–Hilliard (CH) equation is a classical mathematical equation which models the spinodal decomposition in binary fluid mixtures. In the real world, the phase change in a two-phase system usually occurs in irregular domains. To efficiently and accurately simulate this dynamics, we herein develop linear temporally first- and second-order accurate methods for the CH equation in arbitrary domains. The implicit-explicit (IMEX) Runge–Kutta method is adopted to construct discrete schemes in time. By introducing a simple boundary control function, we transform the original equations into equivalent forms in irregular domains and discretize the space by using the standard second-order finite difference stencil. In each temporal step, the proposed numerical schemes are highly efficient and easy to implement because we only need to solve several linear elliptic type equations. The mass conservation and unconditional energy stability of the proposed schemes are analytically proved. The multigrid algorithm is adopted for fast computation. The numerical results confirm the desired accuracy in time and space, mass conservation, and energy dissipation property. Moreover, the extensive calculations in two- and three-dimensional spaces indicate that the proposed method has good capability to simulate spinodal decomposition in arbitrarily irregular domains.

1. Introduction

The phase-field method is a popular mathematical tool to describe many problems related to interfacial changes or phase transitions, see [1–3] for particular applications. Most phase-field models are derived from the total free energy functionals of the governing systems. If we consider a system without the effect of an external force, then the solutions of phase-field models will dissipate the total energy. This property corresponds to the second law of thermodynamics. Therefore, the phase-field method is physically meaningful. The Cahn–Hilliard (CH) equation is a classical phase-field model, which was originally developed by Cahn and Hilliard [4] to describe the spinodal decomposition in binary fluid mixtures. For the detailed description of the physical, mathematical, and numerical derivations of the CH equation, please refer to [5]. For the applications of the CH equation in practical problems, such as two-phase fluid flows, topology optimization, tumor growth, and image inpainting, see [6]. In a bounded, smooth, and connected domain Ω , we consider the following total free energy functional:

$$E(\phi) = \int_{\Omega} \left(F(\phi) + \frac{\epsilon^2}{2} |\nabla \phi|^2 \right) dx, \quad (1)$$

where $\phi = \phi(x, t)$ is the phase-field variable (or order parameter) which is used to distinguish two immiscible fluid materials. The nonlinear potential accounting for phase separation is $F(\phi) = 0.25(\phi^2 - 1)^2$. We assume $\phi = 1$ and -1 in the bulk regions of different components. The value of ϕ changes smoothly from -1 to 1 across the interface between two materials. The thickness of this transition layer is related to the small positive constant ϵ . The nonlinear potential can be split into $F_a(\phi) = \phi^4/4 - (1+r)\phi^2/2 + 1/4$ and $F_b(\phi) = r\phi^2/2$. Here, $r > 0$ is a constant. The original total energy functional can be expressed as the following equivalent form:

* Corresponding author.

E-mail address: yangjx79@mail.sysu.edu.cn (J. Yang).

$$E(\phi) = \int_{\Omega} \left(F_a(\phi) + F_b(\phi) + \frac{\epsilon^2}{2} |\nabla \phi|^2 \right) d\mathbf{x}. \quad (2)$$

As a gradient flow of the total energy functional, Eq. (2), the CH model can be written as follows:

$$\frac{\partial \phi}{\partial t} = M \Delta \mu, \quad (3)$$

$$\mu = f(\phi) + r\phi - \epsilon^2 \Delta \phi, \quad (4)$$

where $\mu = \delta E(\phi)/\delta \phi$ is the chemical potential and $f(\phi) = F'_a(\phi) = \phi^3 - (1+r)\phi$. Here, $M > 0$ is the mobility and we assume it is a constant for convenience. The zero Neumann boundary condition is applied, i.e., $\mathbf{n} \cdot \nabla \phi|_{\partial\Omega} = \mathbf{n} \cdot \nabla \mu|_{\partial\Omega} = 0$, where \mathbf{n} is the unit outward normal vector to the boundary of full domain, $\partial\Omega$. Note that the CH equation generally does not satisfy the maximum principle (i.e., the value of ϕ is not bounded by -1 and 1). Now, we introduce a truncated form of $f(\phi)$ [7], i.e.,

$$\tilde{f}(\phi) = \begin{cases} \phi^3 - \phi - r\phi, & \text{if } |\phi| \leq \mathcal{M}, \\ (3\mathcal{M}^2 - 1)\phi - 2\mathcal{M}^3 - r\phi, & \text{otherwise.} \end{cases} \quad (5)$$

Here, the threshold value \mathcal{M} is large than 1 . It can be observed that the original form of $f(\phi)$ makes $f'(\phi)$ be not upper bounded, the truncation from in Eq. (5) fixes this problem and facilitates the construction of linear energy-stable time-marching scheme. For the applications of truncation on the CH models, see [8,9] and references therein. Furthermore, this truncation has also been used for the Swift–Hohenberg (SH) [10] and phase-field crystal (PFC) [11] phase-field models. In this work, we adopt the above truncated form and drop the superscript \sim for convenience. By taking the time derivative of Eq. (1) with respect to time t , we have

$$\begin{aligned} \frac{d}{dt} E(\phi) &= \int_{\Omega} (f(\phi)\phi_t + \epsilon^2 \nabla \phi \cdot \nabla \phi_t) d\mathbf{x} = \int_{\Omega} (f(\phi) - \epsilon^2 \Delta \phi) \phi_t d\mathbf{x} + \epsilon^2 \int_{\partial\Omega} \phi_t \mathbf{n} \cdot \nabla \phi ds \\ &= \int_{\Omega} \mu \Delta \mu d\mathbf{x} = - \int_{\Omega} |\nabla \mu|^2 d\mathbf{x} \leq 0, \end{aligned} \quad (6)$$

where the homogeneous boundary condition is used. The above inequality indicates the energy dissipation property of the CH equation. By taking the time derivative to the total mass, $\int_{\Omega} \phi d\mathbf{x}$, we obtain

$$\frac{d}{dt} \int_{\Omega} \phi d\mathbf{x} = \int_{\Omega} \frac{\partial \phi}{\partial t} d\mathbf{x} = M \int_{\Omega} \Delta \mu d\mathbf{x} = M \int_{\partial\Omega} \mathbf{n} \cdot \nabla \mu ds = 0. \quad (7)$$

From the above equality, we know that the mass conservation is another basic property of the CH equation.

With the development of computational techniques, the numerical simulation has been a popular approach to study the dynamics of the CH equation, please refer to [12–16] for typical numerical researches based on finite difference method (FDM), spectral method, and lattice Boltzmann method. To preserve the properties of energy dissipation and mass conservation at numerical level, Eyre [17] developed the famous nonlinear convex splitting method with first-order accuracy in time. Based on the convex splitting idea, Yan et al. [18] proposed a temporally second-order accurate and unconditionally energy-stable nonlinear scheme for the CH equation. Based on the fourth-order finite difference stencil in space and second-order convex splitting in time, Cheng et al. [19] developed a provably energy-stable compact scheme for the CH equation. For the CH model with logarithmic potential, Chen et al. [20] developed positivity-preserving and unconditionally stable convex splitting algorithm. For the CH type fluid systems and CH type surfactant system, the mass-conserved and energy-stable nonlinear convex splitting algorithms were developed [21–23]. The detailed error and convergence estimations of the numerical schemes for the CH model can be found in [24–27] and references therein. Furthermore, the nonlinear convex splitting method has been widely used to develop temporally high-order accurate and energy-stable methods for other phase-field models, such as the Swift–Hohenberg (SH) equation [28] and phase-field crystal (PFC) equation [29,30]. Different from the nonlinear convex splitting, the linear convex splitting treats the nonlinear terms in an explicit manner and introduces an appropriate stabilizer to satisfy the convexity. Based on the linear convex splitting, Lee [10] developed a non-iterative scheme with unconditional energy stability for the SH model. By combining with linear splitting method and strong stability-preserving (SSP) approach, Song [31] designed first- and second-order time-accurate methods for the binary CH equation. Similar with the linear splitting scheme, the linear stabilization scheme [8,32] and energy factorization scheme [33,34] are practical for phase-field problems. Moreover, recently developed Energy Quadratization (EQ) [35–37] and Scalar Auxiliary Variable (SAV) [38,39] methods also provide interesting approaches to design structure-preserving schemes for the CH type models.

Although there have been numerous numerical algorithms for simulating the CH model, most of them are limited to regular domains. Actually, the spinodal decomposition or flow coupled phase separations occur inside irregular regions in real applications. The geometry of irregular domain also affects the evolutional dynamics. Therefore, we need to develop a practical numerical method to simulate the CH model in arbitrary domains with complex shapes. For the CH equation in complex domains, a simple approach is to consider a ternary CH system and fix one component as irregular regions [40–42]. During the evolution, the fixed component always keeps the initial state. Thus, the evolution of other two components is naturally constrained in the irregular domains. Based on this approach, Liu et al. [43] calculated the fluid-structure interaction in which the no-slip condition on the solid boundary was achieved by the immersed boundary method (IBM). Later, this kind of treatment was extended to compute three-dimensional two-phase fluid flows with moving contact line in irregular domains [44]. It should be noted that this approach still leads to the overlap across the solid phase and liquid phase. Furthermore, the energy dissipation law with respect to the original CH energy, Eq. (1) was not analytically proved in [40,41].

To avoid the formation of overlapped phases, the authors in [45] transformed the original CH equation into the complex domain by introducing a boundary indicator. The first-order linear splitting scheme was adopted in their work to perform discretization in time. Although the discrete version of mass conservation was proved, the analytical energy estimation was not proved. In the present work, we developed novel fully discrete schemes by combining the FDM in space and linear IMEX Runge–Kutta approaches in time. A simple boundary control function is introduced to construct an equivalent CH model in irregular regions. Because of the property of boundary control function at discrete version, the proofs of mass conservation and unconditional energy stability can be rigorously established. Furthermore, the proposed schemes are efficient and easy to implement because we only need to solve several linear elliptic type equations in each time step. To our best knowledge, this is the first work focusing on efficiently

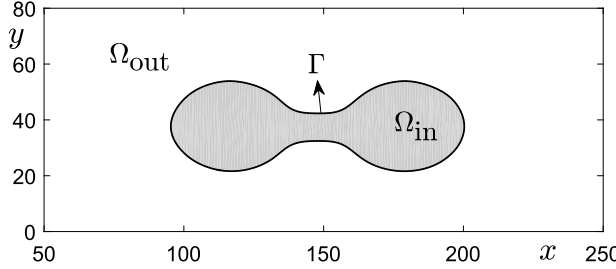


Fig. 1. Schematic illustrations of irregular domain Ω_{in} , exterior region Ω_{out} , and irregular boundary Γ .

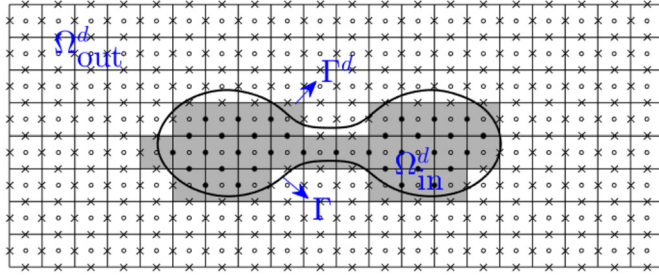


Fig. 2. Shaped region is Ω_{in}^d , the boundary of shaped region is Γ^d . The value of G_{ij} at points (\bullet, o) and (x, o) is one and zero, respectively.

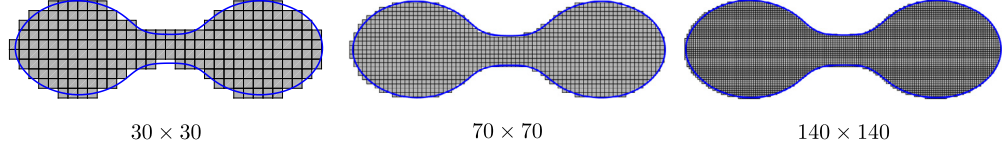


Fig. 3. The continuous irregular domain Ω_{in} is approximated by Ω_{in}^d with the refinement of mesh size h . The mesh size is shown under each figure.

linear, second-order accurate, and fully discrete finite difference methods with provable energy stability for the CH equation in arbitrarily irregular domains.

The remainder of this article is organized as follows. In Section 2, the fully discrete numerical schemes are present. The discrete versions of mass conservation and energy stability are analytically proved. In Section 3, we perform extensive numerical simulations to validate the accuracy, stability, and capability of the proposed schemes. In Section 4, the conclusions are drawn.

2. Fully discrete numerical schemes

In this section, we let the arbitrarily complex domain Ω_{in} be embedded into a regular domain Ω . The boundary of Ω_{in} is denoted by Γ . The schematic illustration is shown in Fig. 1. We define a boundary control function $C = C(\mathbf{x})$ and let $C = 1$ in Ω_{in} and $C = 0$ in $\Omega_{out} = \Omega / \Omega_{in}$. In Ω_{in} , the original equations, Eqs. (3)–(4), can be recast to be

$$\frac{\partial \phi}{\partial t} = \nabla \cdot (MC\nabla\mu), \quad (8)$$

$$\mu = f(\phi) + r\phi - \epsilon^2 \nabla \cdot (C\nabla\phi). \quad (9)$$

It can be observed that Eqs. (8)–(9) and Eqs. (3)–(4) are equivalent in the irregular domain. In Ω_{out} , Eqs. (8) and (9) do not evolve. On the boundary of irregular domain, i.e., Γ , we have

$$C\nabla\phi = C\nabla\mu = \mathbf{0},$$

which indicates that the homogeneous Neumann boundary can be assumed on Γ .

To propose the computational schemes for solving the CH equation in irregular domains, the FDM is used to discretize the computational domain. For convenience, we only describe the discretization in two-dimensional (2D) space, the extension to three-dimensional (3D) space is straightforward. Let a full domain (rectangular domain) be $\Omega = (0, L_x) \times (0, L_y)$. The uniform mesh size is defined as $h = L_x/N_x = L_y/N_y$, where N_x and N_y are positive integers. The discrete version of full domain is $\Omega^d = \{(x_i, y_j) : x_i = (i - 0.5)h, y_j = (j - 0.5)h\}$, where $1 \leq i \leq N_x$ and $1 \leq j \leq N_y$. The uniform time step is defined as $\Delta t = T/N_t$, where T is the total computational time, N_t is the number of time iteration. Let ϕ_{ij}^n and μ_{ij}^n be the approximations of $\phi(x_i, y_j, n\Delta t)$ and $\mu(x_i, y_j, n\Delta t)$, respectively. The discrete boundary control function is defined as C_{ij} , we let $C_{ij} = 1$ in Ω_{in}^d and $C_{ij} = 0$ in Ω_{out}^d . Here, the discrete irregular domain and exterior region are defined as $\Omega_{in}^d = \Omega^d \cap \Omega_{in}$ and $\Omega_{out}^d = \Omega^d \cap \Omega_{out}$, respectively. At the cell edges, we define $G_{i+\frac{1}{2},j} = G_{ij}G_{i+1,j}$ and $G_{i,j+\frac{1}{2}} = G_{ij}G_{i,j+1}$. The schematic illustrations of discrete irregular domain Ω_{in}^d , discrete staggered boundary Γ^d , and the distribution of G_{ij} are shown in Fig. 2. As we refine the grid size, the discrete irregular domain Ω_{in}^d converges to Ω_{in} , see Fig. 3.

The semi-discrete scheme for the CH equation in space can be postulated as

$$\frac{\partial \phi_{ij}}{\partial t} = \nabla_d \cdot (MC_{ij}\nabla_d\mu_{ij}), \quad (10)$$

$$\mu_{ij} = f(\phi_{ij}) + r\phi_{ij} - \epsilon^2 \nabla_d \cdot (C_{ij} \nabla_d \phi_{ij}). \quad (11)$$

If $\mathbf{x}_{i+\frac{1}{2},j}$ is the point locating on the discrete staggered boundary Γ^d , then we have

$$C_{i+\frac{1}{2},j} \nabla_d \phi_{i+\frac{1}{2},j} = 0 \text{ and } C_{i+\frac{1}{2},j} \nabla_d \mu_{i+\frac{1}{2},j} = 0$$

because $C_{i+\frac{1}{2},j} = 0$. If $\mathbf{x}_{i,j+\frac{1}{2}}$ is the point locating on the discrete staggered boundary Γ^d , the similar conclusions are obtained. Therefore, the discrete version of homogeneous Neumann boundary condition on Γ^d can be assumed. The discrete gradient operators are defined to be

$$D_x \phi_{i+\frac{1}{2},j} = \frac{\phi_{i+1,j} - \phi_{ij}}{h} \text{ and } D_x \phi_{i,j+\frac{1}{2}} = \frac{\phi_{i,j+1} - \phi_{ij}}{h}.$$

On the boundaries of discrete full domain Ω^d , we impose the following homogeneous Neumann boundary condition

$$D_x \phi_{\frac{1}{2},j} = D_x \phi_{N_x+\frac{1}{2},j} = D_y \phi_{i,\frac{1}{2}} = D_y \phi_{i,N_y+\frac{1}{2}} = 0.$$

The discrete divergence operator is defined to be

$$\begin{aligned} \nabla_d \cdot (C_{ij} \nabla_d \phi_{ij}) &= \frac{C_{i+\frac{1}{2},j} (\phi_{i+1,j} - \phi_{ij}) - C_{i-\frac{1}{2},j} (\phi_{ij} - \phi_{i-1,j})}{h^2} \\ &\quad + \frac{C_{i,j+\frac{1}{2}} (\phi_{i,j+1} - \phi_{ij}) - C_{i,j-\frac{1}{2}} (\phi_{ij} - \phi_{i,j-1})}{h^2}. \end{aligned}$$

For two arbitrary discrete functions ψ_{ij} and ρ_{ij} , we define the discrete L^2 -inner products in a discrete irregular domain Ω_{in}^d as

$$(\psi, \rho)_d = h^2 \sum_{i=1}^{N_x} \sum_{j=1}^{N_y} C_{ij} \psi_{ij} \rho_{ij}, \quad (12)$$

$$(\nabla_d \psi, \nabla_d \rho)_e = h^2 \left(\sum_{i=0}^{N_x} \sum_{j=1}^{N_y} C_{i+\frac{1}{2},j} D_x \psi_{i+\frac{1}{2},j} D_x \rho_{i+\frac{1}{2},j} + \sum_{i=1}^{N_x} \sum_{j=0}^{N_y} C_{i,j+\frac{1}{2}} D_y \psi_{i,j+\frac{1}{2}} D_y \rho_{i,j+\frac{1}{2}} \right). \quad (13)$$

The discrete L^2 -norms related to ψ_{ij} and $\nabla_d \psi_{ij}$ are $\|\psi\|_d^2 = (\psi, \psi)_d$ and $\|\nabla_d \psi\|_e^2 = (\nabla_d \psi, \nabla_d \psi)_e$. To simplify the notations, we let

$$\sum_{C_{ij}=1} = \sum_{i=1}^{N_x} \sum_{j=1}^{N_y} C_{ij}, \quad \sum_{C_{i+\frac{1}{2},j}=1} = \sum_{i=0}^{N_x} \sum_{j=1}^{N_y} C_{i+\frac{1}{2},j}, \quad \sum_{C_{i,j+\frac{1}{2}}=1} = \sum_{i=1}^{N_x} \sum_{j=0}^{N_y} C_{i,j+\frac{1}{2}}. \quad (14)$$

Theorem 2.1. From the definitions of discrete boundary control function and L^2 -inner products, the following relation holds

$$(\psi, \nabla_d \cdot (C \nabla_d \rho))_d = -(\nabla_d \psi, \nabla_d \rho)_e. \quad (15)$$

Proof. By using the definitions in Eq. (14), we have

$$\begin{aligned} (\psi, \nabla_d \cdot (C \nabla_d \rho))_d &= \sum_{C_{ij}=1} \psi_{ij} \nabla_d \cdot (C_{ij} \nabla_d \rho_{ij}) \\ &= \sum_{C_{ij}=1} \left(\psi_{ij} C_{i+\frac{1}{2},j} \frac{\rho_{i+1,j} - \rho_{ij}}{h^2} - \psi_{ij} C_{i-\frac{1}{2},j} \frac{\rho_{ij} - \rho_{i-1,j}}{h^2} \right) \\ &\quad + \sum_{C_{ij}=1} \left(\psi_{ij} C_{i,j+\frac{1}{2}} \frac{\rho_{i,j+1} - \rho_{ij}}{h^2} - \psi_{ij} C_{i,j-\frac{1}{2}} \frac{\rho_{ij} - \rho_{i,j-1}}{h^2} \right) \\ &= \sum_{C_{i+\frac{1}{2},j}=1} \left(\frac{\psi_{ij} D_x \rho_{i+\frac{1}{2},j}}{h} \right) - \sum_{C_{i-\frac{1}{2},j}=1} \left(\frac{\psi_{ij} D_x \rho_{i-\frac{1}{2},j}}{h} \right) \\ &\quad + \sum_{C_{i,j+\frac{1}{2}}=1} \left(\frac{\psi_{ij} D_y \rho_{i,j+\frac{1}{2}}}{h} \right) - \sum_{C_{i,j-\frac{1}{2}}=1} \left(\frac{\psi_{ij} D_y \rho_{i,j-\frac{1}{2}}}{h} \right) \\ &= \sum_{C_{i+\frac{1}{2},j}=1} \left(\frac{\psi_{ij} D_x \rho_{i+\frac{1}{2},j}}{h} \right) - \sum_{C_{i+\frac{1}{2},j}=1} \left(\frac{\psi_{i+1,j} D_x \rho_{i+\frac{1}{2},j}}{h} \right) \\ &\quad + \sum_{C_{i,j+\frac{1}{2}}=1} \left(\frac{\psi_{ij} D_y \rho_{i,j+\frac{1}{2}}}{h} \right) - \sum_{C_{i,j+\frac{1}{2}}=1} \left(\frac{\psi_{i,j+1} D_y \rho_{i,j+\frac{1}{2}}}{h} \right) \\ &= - \sum_{C_{i+\frac{1}{2},j}=1} \left(D_x \psi_{i+\frac{1}{2},j} D_x \rho_{i+\frac{1}{2},j} \right) - \sum_{C_{i,j+\frac{1}{2}}=1} \left(D_y \psi_{i,j+\frac{1}{2}} D_y \rho_{i,j+\frac{1}{2}} \right) = -(\nabla_d \psi, \nabla_d \rho)_e. \end{aligned}$$

The proof is completed. \square

Note that the above relation will be used in the following contents in this section.

2.1. Temporally first-order accurate scheme

Based on the SSP-IMEX RK approach, the authors in [31] pointed that the one-step and two-step linear discretization in time could lead to temporally first-order accurate schemes. We note that the well-known linear convex splitting method [17] is a typical one-step discretization in time. Different from the scheme proposed in [45], we herein provide an alternative scheme by combining the two-step IMEX RK method in time and the FDM in space. The fully discrete scheme consists of the following two steps

Step 1. With the known ϕ_{ij}^n , we update ϕ_{ij}^* from the following equations

$$\phi_{ij}^* = \phi_{ij}^n + \Delta t \nabla_d \cdot (MC_{ij} \nabla_d \mu_{ij}^*), \quad (16)$$

$$\mu_{ij}^* = f(\phi_{ij}^n) + r\phi_{ij}^* - \epsilon^2 \nabla_d \cdot (C_{ij} \nabla_d \phi_{ij}^*). \quad (17)$$

Step 2. With computed ϕ_{ij}^n and ϕ_{ij}^* , we update ϕ^{n+1} from the following equations

$$\phi_{ij}^{n+1} = \frac{1}{2} \phi_{ij}^n + \frac{1}{2} \phi_{ij}^* + \frac{\Delta t}{2} \nabla_d \cdot (MC_{ij} \nabla_d \mu_{ij}^{n+1}), \quad (18)$$

$$\mu_{ij}^{n+1} = f(\phi_{ij}^*) + r\phi_{ij}^{n+1} - \epsilon^2 \nabla_d \cdot (C_{ij} \nabla_d \phi_{ij}^{n+1}). \quad (19)$$

Theorem 2.2. The solutions in Step 1 and Step 2 satisfy the mass conservation, i.e., $(\phi^*, \mathbf{1})_d = (\phi^n, \mathbf{1})_d$ and $(\phi^{n+1}, \mathbf{1})_d = (\phi^n, \mathbf{1})_d$.

Proof. By taking the discrete L^2 -inner product of Eq. (16) with $\mathbf{1}$, we get

$$\begin{aligned} (\phi^*, \mathbf{1})_d &= (\phi^n, \mathbf{1})_d + \Delta t (\nabla_d \cdot (MC \nabla_d \mu^*), \mathbf{1})_d \\ &= (\phi^n, \mathbf{1})_d - \Delta t (MC \nabla_d \mu^*, \nabla_d \mathbf{1})_e = (\phi^n, \mathbf{1})_d. \end{aligned} \quad (20)$$

Here, the conclusion in Theorem 2.1 is used. By taking the discrete L^2 -inner product of Eq. (18) with $\mathbf{1}$, we get

$$\begin{aligned} (\phi^{n+1} - \phi^n, \mathbf{1})_d &= \frac{1}{2} (\phi^* - \phi^n, \mathbf{1})_d + \frac{\Delta t}{2} (\nabla_d \cdot (MC \nabla_d \mu^{n+1}), \mathbf{1})_d \\ &= \frac{1}{2} (\phi^* - \phi^n, \mathbf{1})_d - \Delta t (MC \nabla_d \mu^{n+1}, \nabla_d \mathbf{1})_e = \frac{1}{2} (\phi^* - \phi^n, \mathbf{1})_d = 0. \end{aligned} \quad (21)$$

The above equality indicates $(\phi^{n+1}, \mathbf{1})_d = (\phi^n, \mathbf{1})_d$. The proof is completed. \square

Theorem 2.3. With $M = 1.2$ and $r \geq 4.32$, the following energy inequality unconditionally holds

$$E(\phi^{n+1}) \leq E(\phi^n), \quad (22)$$

where the discrete energy in Ω_{in}^d at n -th temporal level is given as

$$E(\phi^n) = (F_a(\phi^n), \mathbf{1})_d + \frac{r}{2} \|\phi^n\|_d^2 + \frac{\epsilon^2}{2} \|\sqrt{C} \nabla_d \phi^n\|_e^2.$$

Proof. By multiplying Eq. (16) with μ_{ij}^* and taking the discrete L^2 -inner product, we have

$$(\phi^* - \phi^n, \mu^*)_d = \Delta t (\nabla_d \cdot (MC \nabla_d \mu^*), \mu^*)_d = -M \Delta t \|\sqrt{C} \nabla_d \mu^*\|_e^2, \quad (23)$$

where the conclusion in Theorem 2.1 is used. By multiplying Eq. (17) with $\phi_{ij}^* - \phi_{ij}^n$ and taking the discrete L^2 -inner product, we have

$$\begin{aligned} (\mu^*, \phi^* - \phi^n)_d &= \underbrace{(f(\phi^n), \phi^* - \phi^n)_d}_{\text{I}} + \frac{r}{2} (\|\phi^*\|_d^2 - \|\phi^n\|_d^2 + \|\phi^* - \phi^n\|_d^2) \\ &\quad + \frac{\epsilon^2}{2} (\|\sqrt{C} \nabla_d \phi^*\|_e^2 - \|\sqrt{C} \nabla_d \phi^n\|_e^2 + \|\sqrt{C} \nabla_d (\phi^* - \phi^n)\|_e^2), \end{aligned} \quad (24)$$

where the equality $(p, p - q) = \frac{1}{2} [p^2 - q^2 + (p - q)^2]$ is used. By the Taylor expansion, the term I is expressed to be

$$(f(\phi^n), \phi^* - \phi^n)_d = (F_a(\phi^*) - F_a(\phi^n), \mathbf{1})_d - \frac{f'(\chi_1)}{2} \|\phi^* - \phi^n\|_d^2, \quad (25)$$

where χ_1 is a constant between ϕ^* and ϕ^n . By combining Eqs. (23)–(25) and dropping some positive terms, we derive

$$E(\phi^*) - E(\phi^n) + \frac{r}{2} \|\phi^* - \phi^n\|_d^2 \leq \frac{f'(\chi_1)}{2} \|\phi^* - \phi^n\|_d^2. \quad (26)$$

By multiplying Eq. (18) with μ_{ij}^{n+1} and taking the discrete L^2 -inner product, we have

$$(\phi^{n+1} - \phi^n, \mu^{n+1})_d = (\phi^* - \phi^{n+1}, \mu^{n+1})_d - M \Delta t \|\sqrt{C} \nabla_d \mu^{n+1}\|_e^2. \quad (27)$$

By multiplying Eq. (19) with $\phi_{ij}^{n+1} - \phi_{ij}^*$ and taking the discrete L^2 -inner product, we get

$$\begin{aligned} (\mu^{n+1}, \phi^{n+1} - \phi^*)_d &= (f(\phi^*), \phi^{n+1} - \phi^*)_d + \frac{r}{2} (\|\phi^{n+1}\|_d^2 - \|\phi^*\|_d^2 + \|\phi^{n+1} - \phi^*\|_d^2) \\ &\quad + \frac{\epsilon^2}{2} (\|\sqrt{C} \nabla_d \phi^{n+1}\|_e^2 - \|\sqrt{C} \nabla_d \phi^*\|_e^2 + \|\sqrt{C} \nabla_d (\phi^{n+1} - \phi^*)\|_e^2). \end{aligned} \quad (28)$$

By following the same procedures in (23)–(26), we rewrite the above equality to be

$$\begin{aligned} (\mu^{n+1}, \phi^{n+1} - \phi^*)_d &= E(\phi^{n+1}) - E(\phi^*) + \frac{r}{2} \|\phi^{n+1} - \phi^*\|_d^2 + \frac{\epsilon^2}{2} \|\sqrt{C} \nabla_d (\phi^{n+1} - \phi^*)\|_e^2 \\ &\quad - \frac{f'(\chi_2)}{2} \|\phi^{n+1} - \phi^*\|_d^2. \end{aligned} \quad (29)$$

By multiplying Eq. (19) with $\phi_{ij}^{n+1} - \phi_{ij}^n$ and taking the discrete L^2 -inner product, we get

$$\begin{aligned} (\mu^{n+1}, \phi^{n+1} - \phi^n)_d &= (f(\phi^*), \phi^{n+1} - \phi^n)_d + \frac{r}{2} (\|\phi^{n+1}\|_d^2 - \|\phi^n\|_d^2 + \|\phi^{n+1} - \phi^n\|_d^2) \\ &\quad + \frac{\epsilon^2}{2} (\|\sqrt{C} \nabla_d \phi^{n+1}\|_e^2 - \|\sqrt{C} \nabla_d \phi^n\|_e^2 + \|\sqrt{C} \nabla_d (\phi^{n+1} - \phi^n)\|_e^2). \end{aligned} \quad (30)$$

By using the Taylor expansion, we have

$$\begin{aligned} F_a(\phi_{ij}^{n+1}) - F_a(\phi_{ij}^*) &= f(\phi_{ij}^*)(\phi_{ij}^{n+1} - \phi_{ij}^*) + \frac{f'(\chi_2)}{2} (\phi_{ij}^{n+1} - \phi_{ij}^*)^2, \\ F_a(\phi_{ij}^n) - F_a(\phi_{ij}^*) &= f(\phi_{ij}^*)(\phi_{ij}^n - \phi_{ij}^*) + \frac{f'(\chi_3)}{2} (\phi_{ij}^n - \phi_{ij}^*)^2. \end{aligned}$$

By combining the above equalities together and taking the discrete inner product, we have

$$(f(\phi^*), \phi^{n+1} - \phi^n)_d = (F_a(\phi^{n+1}) - F_a(\phi^n), \mathbf{1})_d - \frac{f'(\chi_2)}{2} \|\phi^{n+1} - \phi^*\|_d^2 + \frac{f'(\chi_3)}{2} \|\phi^n - \phi^*\|_d^2. \quad (31)$$

By combining Eqs. (30) and (31), we derive

$$\begin{aligned} (\mu^{n+1}, \phi^{n+1} - \phi^n)_d &= E(\phi^{n+1}) - E(\phi^n) + \frac{r}{2} \|\phi^{n+1} - \phi^n\|_d^2 + \frac{\epsilon^2}{2} \|\sqrt{C} \nabla_d (\phi^{n+1} - \phi^n)\|_e^2 \\ &\quad - \frac{f'(\chi_2)}{2} \|\phi^{n+1} - \phi^*\|_d^2 + \frac{f'(\chi_3)}{2} \|\phi^n - \phi^*\|_d^2. \end{aligned} \quad (32)$$

By combining Eqs. (27), (29), (32), inequality (26), and dropping some unnecessary positive terms, we obtain

$$\begin{aligned} E(\phi^{n+1}) - E(\phi^n) + \underbrace{\frac{1}{2} \left(\frac{r}{2} - \frac{f'(\chi_1)}{2} + \frac{f'(\chi_3)}{2} \right) \|\phi^* - \phi^n\|_d^2}_{\text{I}} + \underbrace{\frac{1}{2} \left(\frac{r}{2} - f'(\chi_2) \right) \|\phi^{n+1} - \phi^*\|_d^2}_{\text{II}} \\ \leq -\frac{M \Delta t}{2} \|\sqrt{C} \nabla_d \mu\|_e^2 \leq 0. \end{aligned} \quad (33)$$

To let the term I be non-negative, we require $r \geq \max(f'(\chi_1)) - \min(f'(\chi_3)) = 3\mathcal{M}^2$. To let term II be non-negative, we require $\frac{r}{2} \geq \max(f'(\chi_2)) = 3\mathcal{M}^2 - 1 - r$. Because $\mathcal{M} = 1.2$ is set, we have $r > 4.32$. The inequality (33) implies the energy is dissipative in time. The proof is completed. \square

2.2. Temporally second-order accurate method

The IMEX RK approach provides a flexible idea to develop temporally second-order accurate method by adding one more calculation step. As mentioned in [31,46], the two-step method is hard to satisfy second-order accuracy and the form of three-step method is not unique. We herein adopt a particular set of coefficients in [46] and design the fully discrete scheme consisting of the three steps

Step 1. With the known ϕ_{ij}^n , we update ϕ_{ij}^* from the following equations

$$\phi_{ij}^* = \phi_{ij}^n + \Delta t \nabla_d \cdot (MC_{ij} \nabla_d \mu_{ij}^*), \quad (34)$$

$$\mu_{ij}^* = f(\phi_{ij}^n) + r\phi_{ij}^* - \epsilon^2 \nabla_d \cdot (C_{ij} \nabla_d \phi_{ij}^*). \quad (35)$$

Step 2. With computed ϕ_{ij}^n and ϕ_{ij}^* , we update ϕ^{n+1} from the following equations

$$\phi_{ij}^{**} = \frac{3}{2} \phi_{ij}^n - \frac{1}{2} \phi_{ij}^* + \frac{\Delta t}{2} \nabla_d \cdot (MC_{ij} \nabla_d \mu_{ij}^{**}), \quad (36)$$

$$\mu_{ij}^{**} = f(\phi_{ij}^*) + r\phi_{ij}^{**} - \epsilon^2 \nabla_d \cdot (C_{ij} \nabla_d \phi_{ij}^{**}). \quad (37)$$

Step 3. With the known ϕ_{ij}^{**} , we update ϕ_{ij}^{n+1} from the following equations

$$\phi_{ij}^{n+1} = \phi_{ij}^{**} + \Delta t \nabla_d \cdot (MC_{ij} \nabla_d \mu_{ij}^{n+1}), \quad (38)$$

$$\mu_{ij}^{n+1} = f(\phi_{ij}^{**}) + r\phi_{ij}^{n+1} - \epsilon^2 \nabla_d \cdot (C_{ij} \nabla_d \phi_{ij}^{n+1}). \quad (39)$$

Theorem 2.4. The solutions in Steps 1, 2, and 3 satisfy the mass conservation, i.e., $(\phi^*, \mathbf{1})_d = (\phi^n, \mathbf{1})_d$, $(\phi^{**}, \mathbf{1})_d = (\phi^n, \mathbf{1})_d$, and $(\phi^{n+1}, \mathbf{1})_d = (\phi^n, \mathbf{1})_d$.

Proof. By taking the discrete L^2 -inner product of Eq. (34) with $\mathbf{1}$, we have

$$(\phi^*, \mathbf{1})_d = (\phi^n, \mathbf{1})_d - \Delta t (MC\nabla_d \mu^*, \nabla_d \mathbf{1})_e = (\phi^n, \mathbf{1})_d. \quad (40)$$

By taking the discrete L^2 -inner product of Eq. (36) with $\mathbf{1}$, we have

$$(\phi^{**} - \phi^n, \mathbf{1})_d = \frac{1}{2} (\phi^n - \phi^*, \mathbf{1})_d - \Delta t (MC\nabla_d \mu^*, \nabla_d \mathbf{1})_e = 0. \quad (41)$$

By taking the discrete L^2 -inner product of Eq. (38) with $\mathbf{1}$, we have

$$(\phi^{n+1}, \mathbf{1})_d = (\phi^{**}, \mathbf{1})_d - \Delta t (MC\nabla_d \mu^*, \nabla_d \mathbf{1})_e = (\phi^{**}, \mathbf{1})_d. \quad (42)$$

Because we have obtained $(\phi^{**}, \mathbf{1})_d = (\phi^n, \mathbf{1})_d$ in Eq. (41). From $(\phi^{n+1}, \mathbf{1})_d = (\phi^{**}, \mathbf{1})_d$ in Eq. (42), we derive $(\phi^{n+1}, \mathbf{1})_d = (\phi^n, \mathbf{1})_d$. The proof is completed. \square

Theorem 2.5. With $M = 1.2$ and $r \geq 9.64$, the following energy inequality unconditionally holds

$$E(\phi^{n+1}) + \frac{3}{2} E(\phi^*) \leq \frac{5}{2} E(\phi^n), \quad (43)$$

Proof. By multiplying μ_{ij}^* to Eq. (34) and taking the discrete L^2 -inner product, we get

$$(\phi^* - \phi^n, \mu^*)_d = \Delta t (\nabla_d \cdot (MC\nabla_d \mu^*), \mu^*)_d = -M\Delta t \|\sqrt{C}\nabla_d \mu^*\|_e^2. \quad (44)$$

By multiplying Eq. (35) with $\phi_{ij}^* - \phi_{ij}^n$ and taking the discrete L^2 -inner product, we have

$$(\mu^*, \phi^* - \phi^n)_d = E(\phi^*) - E(\phi^n) + \frac{r}{2} \|\phi^* - \phi^n\|_d^2 + \frac{\epsilon^2}{2} \|\sqrt{C}\nabla_d(\phi^* - \phi^n)\|_e^2 - \frac{f'(\xi_1)}{2} \|\phi^* - \phi^n\|_d^2, \quad (45)$$

where the discrete summation by parts in Theorem 2 and Taylor expansion are used. By summing Eqs. (44) and (45), we have

$$\begin{aligned} E(\phi^*) - E(\phi^n) &+ \frac{r}{2} \|\phi^* - \phi^n\|_d^2 + \frac{\epsilon^2}{2} \|\sqrt{C}\nabla_d(\phi^* - \phi^n)\|_e^2 - \frac{f'(\xi_1)}{2} \|\phi^* - \phi^n\|_d^2 \\ &= -M\Delta t \|\sqrt{C}\nabla_d \mu^*\|_e^2. \end{aligned} \quad (46)$$

By rewriting Eq. (36), we have

$$\frac{3}{2} (\phi_{ij}^{**} - \phi_{ij}^n) + \frac{1}{2} (\phi_{ij}^* - \phi_{ij}^{**}) = \frac{\Delta t}{2} \nabla_d \cdot (MC_{ij} \nabla_d \mu_{ij}^{**}). \quad (47)$$

By multiplying μ_{ij}^{**} on the above equation and taking the discrete L^2 -inner product, we have

$$\frac{3}{2} (\phi^{**} - \phi^n, \mu^{**})_d + \frac{1}{2} (\phi^* - \phi^{**}, \mu^{**})_d = -\frac{M\Delta t}{2} \|\sqrt{C}\nabla_d \mu^{**}\|_e^2. \quad (48)$$

By multiplying Eq. (37) with $\phi_{ij}^{**} - \phi_{ij}^*$ and performing the discrete L^2 -inner product, we get

$$\begin{aligned} (\mu^{**}, \phi^{**} - \phi^*)_d &= \underbrace{(f(\phi^*), \phi^{**} - \phi^*)_d}_{\text{I}} + \frac{r}{2} (\|\phi^{**}\|_d^2 - \|\phi^*\|_d^2 + \|\phi^{**} - \phi^*\|_d^2) \\ &\quad + \frac{\epsilon^2}{2} \left(\|\sqrt{C}\nabla_d \phi^{**}\|_e^2 - \|\sqrt{C}\nabla_d \phi^*\|_e^2 + \|\sqrt{C}\nabla_d(\phi^{**} - \phi^*)\|_e^2 \right). \end{aligned} \quad (49)$$

By the Taylor expansion, the term I is

$$(f(\phi^*), \phi^{**} - \phi^*)_d = (F_a(\phi^{**}) - F_a(\phi^*), \mathbf{1})_d - \frac{f'(\xi_2)}{2} \|\phi^{**} - \phi^*\|_d^2. \quad (50)$$

Then, Eq. (49) is rewritten to be

$$(\mu^{**}, \phi^{**} - \phi^*)_d = E(\phi^{**}) - E(\phi^*) + \frac{r}{2} \|\phi^{**} - \phi^*\|_d^2 + \frac{\epsilon^2}{2} \|\sqrt{C}\nabla_d(\phi^{**} - \phi^*)\|_e^2 - \frac{f'(\xi_2)}{2} \|\phi^{**} - \phi^*\|_d^2. \quad (51)$$

By multiplying $\phi_{ij}^{**} - \phi_{ij}^*$ on Eq. (37) and performing the discrete L^2 -inner product, we have

$$\begin{aligned} (\mu^{**}, \phi^{**} - \phi^*)_d &= (f(\phi^*), \phi^{**} - \phi^*)_d + \frac{r}{2} (\|\phi^{**}\|_d^2 - \|\phi^*\|_d^2 + \|\phi^{**} - \phi^*\|_d^2) \\ &\quad + \frac{\epsilon^2}{2} \left(\|\sqrt{C}\nabla_d \phi^{**}\|_e^2 - \|\sqrt{C}\nabla_d \phi^*\|_e^2 + \|\sqrt{C}\nabla_d(\phi^{**} - \phi^*)\|_e^2 \right). \end{aligned} \quad (52)$$

By the Taylor expansion, we have

$$F_a(\phi_{ij}^{**}) - F_a(\phi_{ij}^*) = f(\phi_{ij}^*)(\phi_{ij}^{**} - \phi_{ij}^*) + \frac{f'(\xi_2)}{2} (\phi_{ij}^{**} - \phi_{ij}^*)^2,$$

$$F_a(\phi_{ij}^n) - F_a(\phi_{ij}^*) = f(\phi_{ij}^*)(\phi_{ij}^n - \phi_{ij}^*) + \frac{f'(\xi_3)}{2} (\phi_{ij}^n - \phi_{ij}^*)^2.$$

By combining the above equalities together and performing the discrete inner product, we get

$$(f(\phi^*), \phi^{**} - \phi^*)_d = (F_a(\phi^{**}) - F_a(\phi^n), \mathbf{1})_d - \frac{f'(\xi_2)}{2} \|\phi^{**} - \phi^*\|_d^2 + \frac{f'(\xi_3)}{2} \|\phi^n - \phi^*\|_d^2. \quad (53)$$

Then, Eq. (52) is recast to be

$$\begin{aligned} (\mu^{**}, \phi^{**} - \phi^n)_d &= E(\phi^{**}) - E(\phi^n) + \frac{r}{2} \|\phi^{**} - \phi^n\|_d^2 + \frac{\epsilon^2}{2} \|\sqrt{C} \nabla_d (\phi^{**} - \phi^n)\|_e^2 \\ &\quad - \frac{f'(\xi_2)}{2} \|\phi^{**} - \phi^*\|_d^2 + \frac{f'(\xi_3)}{2} \|\phi^n - \phi^*\|_d^2. \end{aligned} \quad (54)$$

By combining Eqs. (48), (51), and (54), the following identity is obtained

$$\begin{aligned} E(\phi^{**}) - \frac{3}{2} E(\phi^n) + \frac{1}{2} E(\phi^*) + \frac{3r}{4} \|\phi^{**} - \phi^n\|_d^2 + \frac{3\epsilon^2}{4} \|\sqrt{C} \nabla_d (\phi^{**} - \phi^n)\|_e^2 \\ - \frac{3f'(\xi_2)}{4} \|\phi^{**} - \phi^*\|_d^2 + \frac{3f'(\xi_3)}{4} \|\phi^n - \phi^*\|_d^2 - \frac{r}{4} \|\phi^{**} - \phi^*\|_d^2 - \frac{\epsilon^2}{4} \|\sqrt{C} \nabla_d (\phi^{**} - \phi^*)\|_e^2 \\ + \frac{f'(\xi_2)}{4} \|\phi^{**} - \phi^*\|_d^2 = -\frac{M\Delta t}{2} \|\sqrt{C} \nabla_d \mu^{**}\|_e^2. \end{aligned} \quad (55)$$

By combining Eqs. (46) and (55) together, we derive

$$\begin{aligned} E(\phi^{**}) - \frac{5}{2} E(\phi^n) + \frac{3}{2} E(\phi^*) + \frac{3r}{4} \|\phi^{**} - \phi^n\|_d^2 + \underbrace{\frac{3\epsilon^2}{4} \|\sqrt{C} \nabla_d (\phi^{**} - \phi^n)\|_e^2}_I \\ \underbrace{\frac{\epsilon^2}{2} \|\sqrt{C} \nabla_d (\phi^* - \phi^n)\|_e^2}_II + \left(\frac{r}{2} - \frac{f'(\xi_1)}{2} + \frac{3f'(\xi_3)}{4} \right) \|\phi^n - \phi^*\|_d^2 + \left(-\frac{r}{4} + \frac{f'(\xi_2)}{4} - \frac{3f'(\xi_2)}{4} \right) \|\phi^{**} - \phi^*\|_d^2 \\ = -\frac{M\Delta t}{2} \|\sqrt{C} \nabla_d \mu^{**}\|_e^2 + \frac{\epsilon^2}{4} \|\sqrt{C} \nabla_d (\phi^{**} - \phi^*)\|_e^2 \\ \leq -\frac{M\Delta t}{2} \|\sqrt{C} \nabla_d \mu^{**}\|_e^2 + \underbrace{\frac{\epsilon^2}{4} \|\sqrt{C} \nabla_d (\phi^{**} - \phi^n)\|_e^2}_III + \underbrace{\frac{\epsilon^2}{4} \|\sqrt{C} \nabla_d (\phi^* - \phi^n)\|_e^2}_IV \end{aligned} \quad (56)$$

Here, the terms III and IV can be absorbed into term I and II, respectively. By multiplying Eq. (38) with μ_{ij}^{n+1} and taking the discrete L^2 -inner product, we have

$$(\phi^{n+1} - \phi^{**}, \mu^{n+1})_d = \Delta t (\nabla_d \cdot (MC \nabla_d \mu^{n+1}), \mu^{n+1})_d = -M\Delta t \|\sqrt{C} \nabla_d \mu^{n+1}\|_e^2. \quad (57)$$

By multiplying Eq. (39) with $\phi_{ij}^{n+1} - \phi_{ij}^{**}$ and taking the discrete L^2 -inner product, we get

$$\begin{aligned} (\mu^{n+1}, \phi^{n+1} - \phi^{**})_d &= (f(\phi^{**}), \phi^{n+1} - \phi^{**})_d + \frac{r}{2} (\|\phi^{n+1}\|_d^2 - \|\phi^{**}\|_d^2 + \|\phi^{n+1} - \phi^{**}\|_d^2) \\ &\quad + \frac{\epsilon^2}{2} (\|\sqrt{C} \nabla_d \phi^{n+1}\|_e^2 - \|\sqrt{C} \nabla_d \phi^{**}\|_e^2 + \|\sqrt{C} \nabla_d (\phi^{n+1} - \phi^{**})\|_e^2). \end{aligned} \quad (58)$$

By the Taylor expansion, we have

$$(f(\phi^{**}), \phi^{n+1} - \phi^{**})_d = (F_a(\phi^{n+1}) - F_a(\phi^{**}), \mathbf{1})_d - \frac{f'(\xi_4)}{2} \|\phi^{n+1} - \phi^{**}\|_d^2. \quad (59)$$

Thus, Eq. (58) are recast to be

$$\begin{aligned} (\mu^{n+1}, \phi^{n+1} - \phi^{**})_d &= E(\phi^{n+1}) - E(\phi^{**}) + \frac{r}{2} \|\phi^{n+1} - \phi^{**}\|_d^2 + \frac{\epsilon^2}{2} \|\sqrt{C} \nabla_d (\phi^{n+1} - \phi^{**})\|_e^2 \\ &\quad - \frac{f'(\xi_4)}{2} \|\phi^{n+1} - \phi^{**}\|_d^2. \end{aligned} \quad (60)$$

By summing Eqs. (57) and (60) together, we have

$$\begin{aligned} E(\phi^{n+1}) - E(\phi^{**}) + \frac{r}{2} \|\phi^{n+1} - \phi^{**}\|_d^2 + \frac{\epsilon^2}{2} \|\sqrt{C} \nabla_d (\phi^{n+1} - \phi^{**})\|_e^2 - \frac{f'(\xi_4)}{2} \|\phi^{n+1} - \phi^{**}\|_d^2 \\ = -M\Delta t \|\sqrt{C} \nabla_d \mu^{n+1}\|_e^2. \end{aligned} \quad (61)$$

By combining Eqs. (56) and (61) and omit unnecessary terms, we obtain

$$\begin{aligned} E(\phi^{n+1}) - \frac{5}{2} E(\phi^n) + \frac{3}{2} E(\phi^*) + \left(\frac{r}{2} - \frac{f'(\xi_4)}{2} \right) \|\phi^{n+1} - \phi^{**}\|_d^2 \\ + \left(\frac{r}{2} - \frac{f'(\xi_1)}{2} + \frac{3f'(\xi_3)}{4} \right) \|\phi^n - \phi^*\|_d^2 - \frac{r}{4} \|\phi^{**} - \phi^*\|_d^2 - \frac{f'(\xi_2)}{2} \|\phi^{**} - \phi^*\|_d^2 \\ \leq -\frac{M\Delta t}{2} \|\sqrt{C} \nabla_d \mu^{n+1}\|_e^2 - M\Delta t \|\sqrt{C} \nabla_d \mu^{n+1}\|_e^2 \end{aligned} \quad (62)$$

By combining the term with same coefficients, we get

$$\begin{aligned} E(\phi^{n+1}) - \frac{5}{2} E(\phi^n) + \frac{3}{2} E(\phi^*) + \underbrace{\left(\frac{r}{2} - \frac{f'(\xi_4)}{2} \right) \|\phi^{n+1} - \phi^{**}\|_d^2}_I + \underbrace{\left(-\frac{r}{4} - \frac{f'(\xi_2)}{2} \right) \|\phi^{**} - \phi^*\|_d^2}_II \end{aligned}$$

Table 1 L^2 -errors and convergence rates of the first-order time-accurate scheme.

Δt :	32 δt	16 δt	8 δt	4 δt	2 δt
Error:	1.38e-4	6.84e-5	3.24e-5	1.39e-5	4.68e-6
Rate:		1.01	1.08	1.22	1.57

Table 2 L^2 -errors and convergence rates of the second-order time-accurate scheme.

Δt :	32 δt	16 δt	8 δt	4 δt	2 δt
Error:	2.56e-5	7.75e-6	2.14e-6	5.58e-7	1.51e-7
Rate:		1.72	1.85	1.94	1.89

$$+ \underbrace{\left(\frac{r}{2} - \frac{f'(\xi_1)}{2} + \frac{3f'(\xi_3)}{4} \right)}_{\text{III}} \|\phi^n - \phi^*\|_d^2 \leq -\frac{M\Delta t}{2} \|\sqrt{C}\nabla_d \mu^{**}\|_e^2 - M\Delta t \|\sqrt{C}\nabla_d \mu^{n+1}\|_e^2 \leq 0. \quad (63)$$

To make term I be non-negative, we require $r \geq \max(f'(\xi_4)) = 3\mathcal{M}^2 - 1 - r$, i.e., $r \geq (3\mathcal{M}^2 - 1)/2$. To make term II be non-negative, we have $-r/4 \geq \max(f'(\xi_2))/2 \geq 0$, i.e., $r > 6\mathcal{M}^2 - 2$. To make term III be non-negative, we require $r/2 \geq f'(\xi_1)/2 - 3f'(\xi_3)/4$, i.e., $r \geq 6\mathcal{M}^2 + 1$. With $\mathcal{M} = 1.2$, we obtain $r \geq 9.64$. The inequality (63) implies the desired result. The proof is completed. \square

Remark 2.1. In this section, we propose fully discrete schemes for solving the CH equation in arbitrarily complex domains. A simple and effective boundary control function is introduced to develop equivalent equations in complex domains. Because of the property of discrete boundary control function, the discrete summation by parts relation holds. By using IMEX RK approaches, we develop linear first- and second-order time-accurate schemes. The mass conservation and unconditionally energy stability can be rigorously proved. Furthermore, the proposed method can directly combine with the efficient multigrid algorithm [47]. Note that the discrete boundary control functions in fine and coarse grids are different and the discrete irregular domains satisfy $\Omega_{in}^d \in \Omega_{in}^D$, where d and D denote the fine and coarse grids, respectively. Therefore, restriction and interpolation operators in multigrid algorithm should be defined in a weighted manner [45]. The present work aims to present an efficient numerical strategy to calculate phase-field model in irregular domains and validate the performance by extensive 2D and 3D simulations. In an upcoming work, we will further investigate the error estimation of the proposed schemes by following the similar idea in [48].

Remark 2.2. For the first-order time-accurate scheme, we obtain the energy law as $E(\phi^{n+1}) \leq E(\phi^n) \leq \dots \leq E(\phi^0)$, where $E(\phi^0)$ is an initial energy. Since $E(\phi^{n+1}) = (F_a(\phi^{n+1}), \mathbf{1})_d + \frac{r}{2} \|\phi^{n+1}\|_d^2 + \frac{\epsilon^2}{2} \|\sqrt{C}\nabla_d \phi^{n+1}\|_e^2$ and $F_a(\phi^{n+1}) = (\phi^{n+1})^4/4 - (1+r)(\phi^{n+1})^2/2 + 1/4$, we have

$$E(\phi^0) \geq \left(\left[\frac{(\phi^{n+1})^2}{2} - \frac{1}{2} \right]^2, \mathbf{1} \right)_d \geq h^2 \left[\frac{(\phi_{ij}^{n+1})^2}{2} - \frac{1}{2} \right]^2$$

for any i and j in 2D space. We then have the uniform boundedness of the numerical solution as $\|\phi^{n+1}\|_\infty \leq \sqrt{1 + 2\sqrt{E(\phi^0)}/h}$. The result in 3D space is straightforward. The uniform boundedness of the solution obtained by the temporally second-order accurate scheme will be left in a separate analytical work.

3. Numerical results

To validate the performance of the proposed schemes, the simulations of CH equation in various complex domains are performed in this section. Without specific needs, we set $M = 0.1$, the full domains are set to be $\Omega = (0, 1) \times (0, 1)$ and $(0, 1) \times (0, 1) \times (0, 1)$ with respect to 2D and 3D cases, respectively. The homogeneous Neumann boundary condition is considered at $\partial\Omega$. Based on the analysis in the previous section, we choose $r = 5$ and $r = 10$ for the temporally first-order and second-order accurate schemes, respectively.

3.1. Convergence in time and energy stability

In the previous section, we analytically proved the discrete versions of energy stability with respect to the temporally first- and second-order accurate methods. To confirm these, we first investigate the convergence rates in time to show the temporal accuracy. The circular computational domain with radius $R = 0.45$ is considered. The initial condition inside Ω_{in} is defined as $\phi(x, y, 0) = \sin(8\pi x)\cos(8\pi y)$. The mesh size $h = 1/128$ is fixed. We set $\epsilon = 0.0075$. Because the exact solution of the CH equation in an irregular domain is difficult to find, the numerical reference solution is obtained by using a finer time step $\delta t = 1.53e-7$. The increasingly larger time steps: $\Delta t = 4\delta t$, $8\delta t$, $16\delta t$, and $32\delta t$ are used to perform the calculations. Let ϕ_{ij}^r and $\phi_{ij}^{\Delta t}$ be reference solution calculated by δt and numerical solution calculated by Δt at (x_i, y_j) . The error is defined to be $e_{ij} = \phi_{ij}^{\Delta t} - \phi_{ij}^r$. Tables 1 and 2 list the L^2 -errors $\|e^{\Delta t}\|_d$ and convergence rates $\log_2 (\|e^{\Delta t}\|_d / \|e^{\Delta t/2}\|_d)$ at $t = 7.8e-5$ with respect to the first-order time-accurate and second-order time-accurate schemes. We can observe that the proposed schemes achieve desired temporal accuracy.

Next, we investigate the evolutions of discrete energy by varying the time step. The initial condition and computational domain are kept unchanged. The numerical computations are performed using the first- and second-order time-accurate methods with mesh size $h = 1/256$. We set $\epsilon = 0.0038$. Figs. 4(a) and (b) plot the energy curves under $\Delta t = 0.25$, 0.05 , and 0.01 with respect to the temporally first-order and second-order methods, respectively. As we can observe, the energy curves are decreasing in time, which indicates that the discrete energy dissipation property is satisfied. In Fig. 4(c), the evolutions of average concentrations $\bar{\phi}$ are displayed with respect to different time steps. The insets show the snapshots calculated by the temporally second-order accurate method. The results indicate that the mass is conserved.

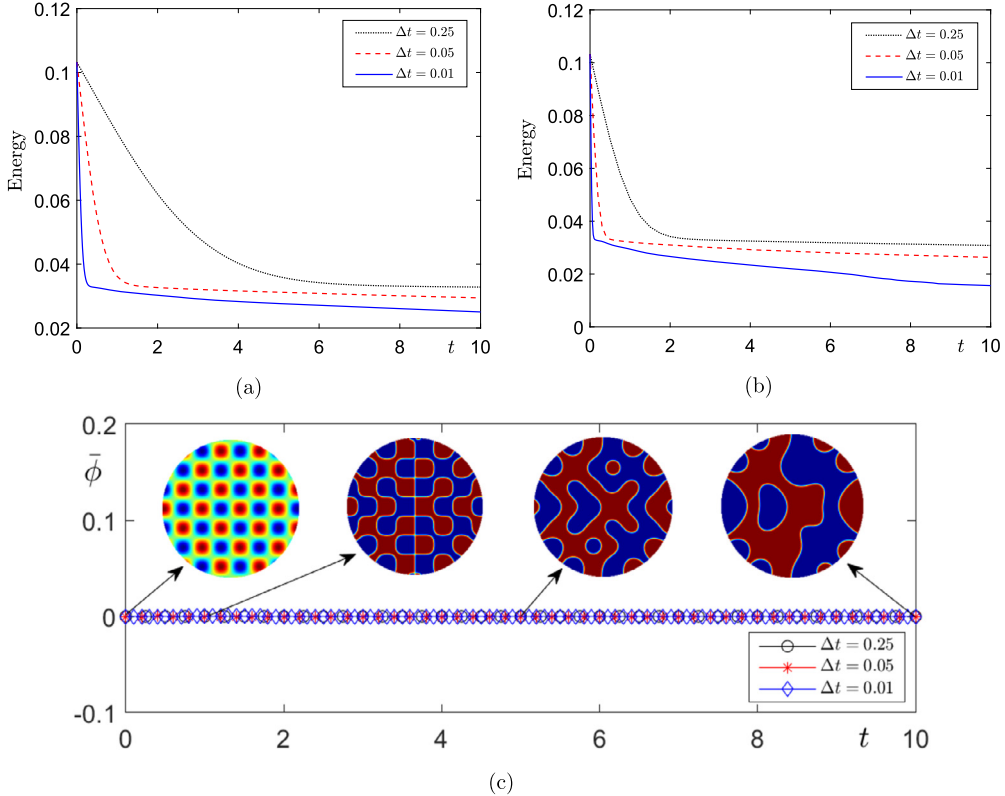


Fig. 4. Evolutions of energy curves with respect to temporally first-order and second-order schemes are plotted in (a) and (b), respectively. The temporal evolutions of average concentrations are shown in (c). The insets display the snapshots at different moments.

Table 3
 L^2 -errors and convergence rates. Here, the temporally first-order accurate scheme is used.

h :	$8h^f$	$4h^f$	$2h^f$
Error:	1.37e-3	3.57e-4	9.33e-5
Rate:		1.94	1.94

Table 4
 L^2 -errors and convergence rates. Here, the temporally second-order accurate scheme is used.

h :	$8h^f$	$4h^f$	$2h^f$
Error:	1.40e-3	3.64e-4	9.44e-5
Rate:		1.94	1.95

3.2. Accuracy in space

To achieve simple and efficient implementation, we develop finite difference scheme to treat the complex domains. The standard central difference stencil is adopted to discretize the spatial operators. To verify the accuracy in space, we fix the time step as $\Delta t = 4.17e-5$. The value of ϵ is set to be 0.04. $\Omega = (0, 2) \times (0, 2)$ is used. Inspired by [45], we consider a region Ω_{out} located within $[0.5, 1.5] \times [0.5, 1.5]$. The following initial condition [45] is defined in $\Omega_{\text{in}} = \Omega / \Omega_{\text{out}}$ as follows:

$$\phi(x, y, 0) = 0.8 \cos(2\pi x) - \cos(2\pi y). \quad (64)$$

A finer mesh size $h^f = 1/256$ is used to obtain the reference solution $\phi_{ij}^{h^f}$ at each point (x_i, y_j) . The calculations are performed by using increasingly larger mesh sizes: $h = 2h^f$, $4h^f$ and $8h^f$ until $t = 8.3e-4$. The error is defined as

$$e_{ij}^{h^f/h} = \phi_{ij}^h - 0.25 \left(\phi_{pi-p/2,pj-p/2}^{h^f} + \phi_{pi-p/2,pj-p/2-1}^{h^f} + \phi_{pi-p/2-1,pj-p/2}^{h^f} + \phi_{pi-p/2-1,pj-p/2-1}^{h^f} \right),$$

where $p = 2, 4$, and 8 , ϕ_{ij}^h is the numerical solution calculated by mesh size h . The L^2 -errors and corresponding rates are defined to be $\|e^{h^f/h}\|_d$ and $\log_2 \left(\|e^{h^f/(2h)}\|_d / \|e^{h^f/h}\|_d \right)$, respectively. Tables 3 and 4 list the errors and convergence rates calculated by the temporally first-order and second-order schemes. The results demonstrate that the proposed scheme achieves the second-order accuracy in space no matter what temporal scheme is used.

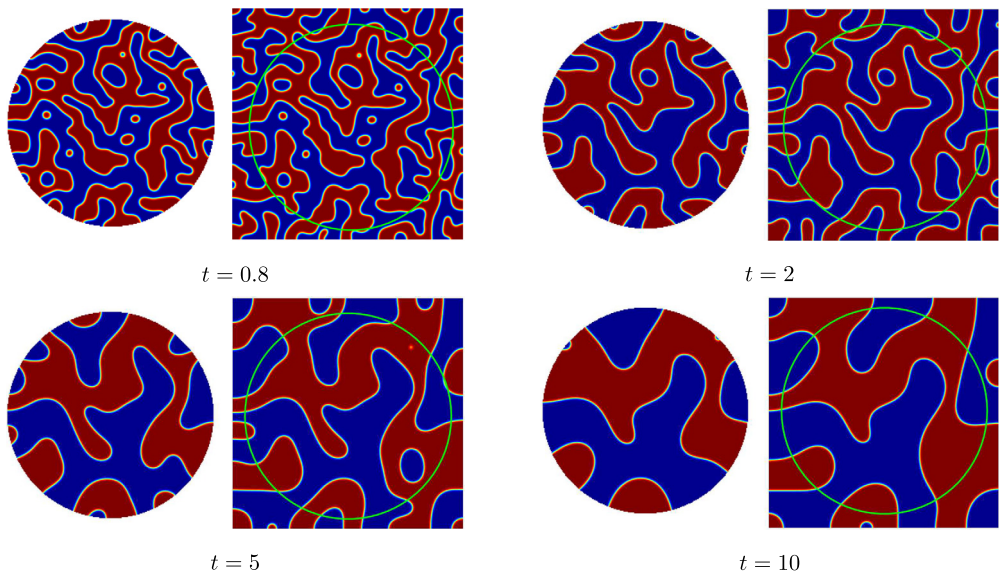


Fig. 5. Snapshots of phase separation in different domains. In each subfigure, the left and right columns display the results in a circular domain and a full domain, respectively.

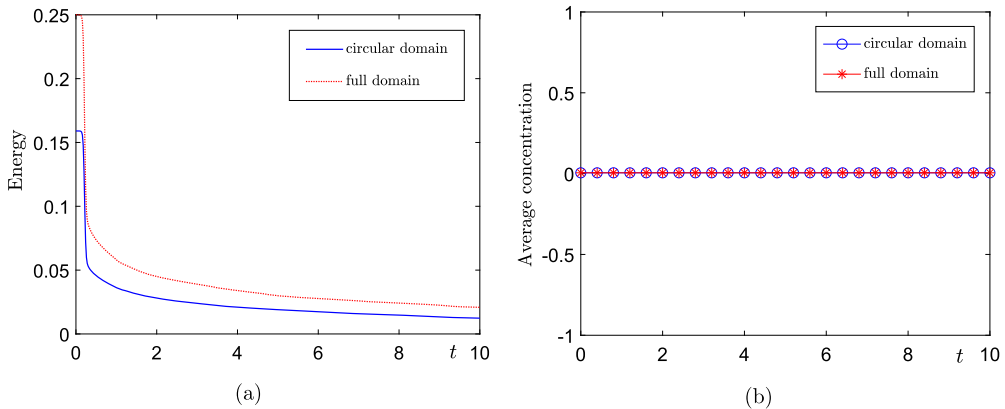


Fig. 6. Evolutions of energy curves (a) and average concentrations (b) in a circular domain and a full domain.



Fig. 7. From the left to right, the subfigures display a dumbbell-shaped domain, a horse-shaped domain, and a complex domain with T-junctions. The experiment of multiple droplets in T-junctions adapted from [49] with permission of APS is shown in the last subfigure.

3.3. Phase separation in circular and full domains

From the discussions in section 2, we know that the discrete boundary control function brings the effect of zero Neumann boundary condition in the neighborhood of irregular boundary. In the region away from the irregular boundary, the evolutional dynamics should not be affected by the boundary shape. To confirm this, we consider a comparison test in which the phase separation is simulated in a circular domain and a full domain, respectively. The initial condition is defined to be

$$\phi(x, y, 0) = 0.01 \text{rand}(x, y), \quad (65)$$

where $\text{rand}(x, y)$ is the number value between -1 and 1 . The time step is $\Delta t = 0.01$, the mesh size is $h = 1/256$, and $\epsilon = 0.0038$. As shown in Fig. 5, the left and right columns display the results in the circular domain with radius $R = 0.45$ and in the full domain. In each full domain, the light green circle is used to represent the area of circular region. In the neighborhood of the boundary of circular domain, we can observe the effect

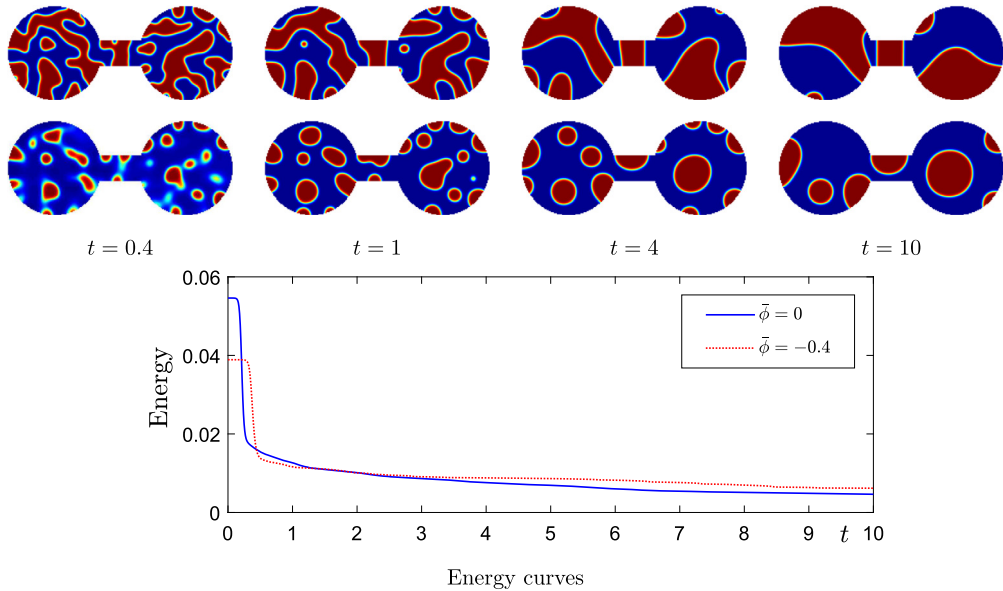


Fig. 8. Spinodal decomposition in a dumbbell-shaped domain. The top and second rows display the snapshots with respect to $\bar{\phi} = 0$ and -0.4 . The last row plots the evolutions of energy.

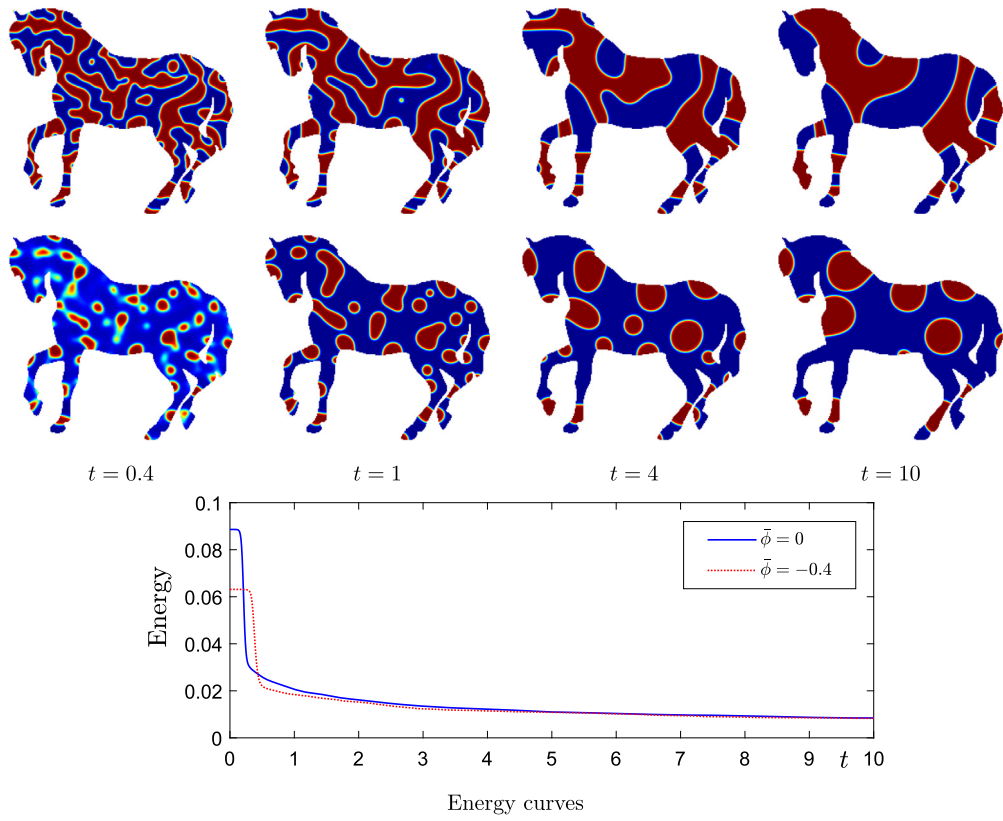


Fig. 9. Spinodal decomposition in a horse-shaped domain. The top and second rows display the snapshots with respect to $\bar{\phi} = 0$ and -0.4 . The last row plots the evolutions of energy.

of homogeneous Neumann boundary condition, i.e., the patterns contact with the boundary in an approximately 90° angle. With time evolution, the same fluid materials merge with each other and gradually occupy most regions. This phase coarsening phenomenon is well simulated in both circular and full domains. In the region away from the irregular boundary (i.e., the central region of the computational domain), we observe that the dynamical behaviors in circular and full domains are almost consistent. In Figs. 6(a) and (b), the temporal evolutions of energy curves and average concentrations are plotted. The results denote that the energy dissipation and mass conservation properties are satisfied.

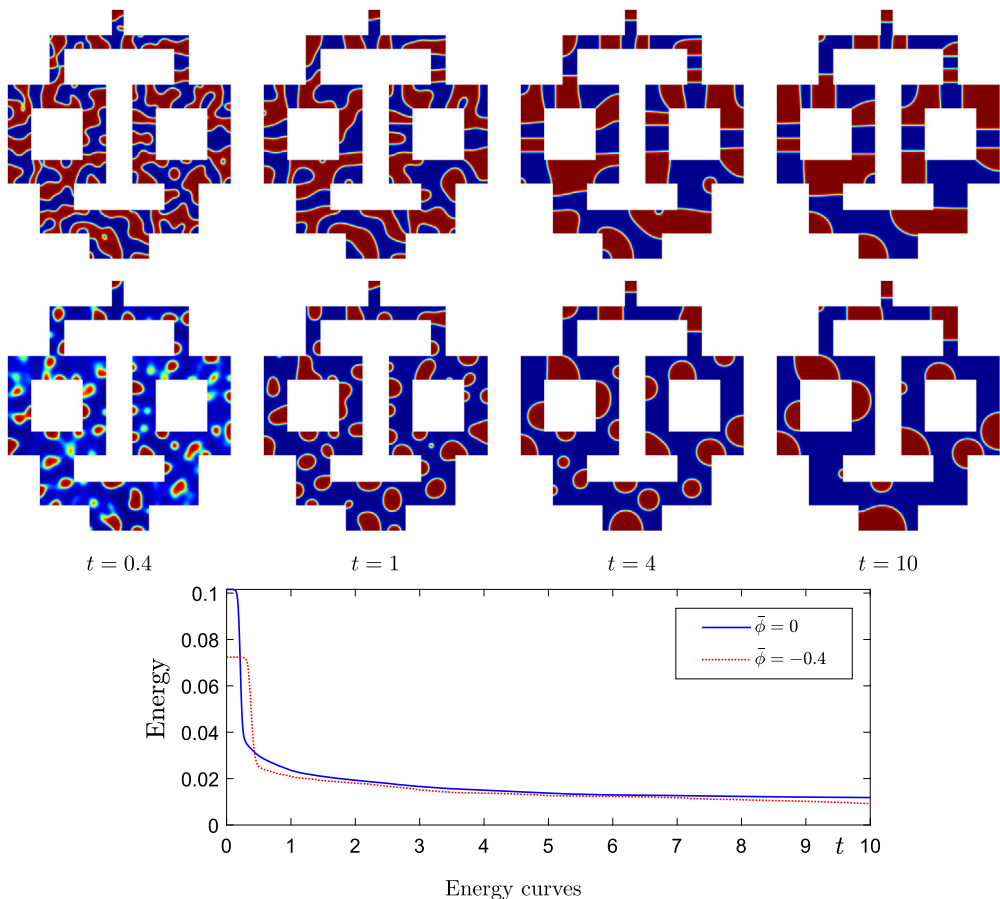


Fig. 10. Spinodal decomposition in a complex domain with T-junctions. The top and second rows display the snapshots with respect to $\bar{\phi} = 0$ and -0.4 . The last row plots the evolutions of energy.

3.4. Spinodal decomposition in two-dimensional irregular domains

The spinodal decomposition is a typical dynamics of CH equation. At initial stage, let us consider two homogeneously distributed fluid materials. With time evolution, the initially small perturbations will lead to the growth of amplitude of ϕ . After the competition between phase separation and phase mixing, the diffuse interface will appear to distinguish two different materials. Subsequently, the same components merge with each other to form bigger patterns until the equilibrium state is arrived. Moreover, the evolution of this coarsening process is significantly affected by the average concentration, see previous simulations [6,16,45].

Now, we compute the spinodal decompositions with different average concentrations in various 2D irregular domains. First of all, we consider the dumbbell-shaped domain, horse-shaped domain, and a domain with T-junctions, see Fig. 7. Note that the T-junctions have been widely used in micro-fluid fields to achieve the accurate control of liquid conversion [49]. The real experiment of multiple droplets in T-junctions is illustrated in the right column of Fig. 7.

The following initial condition is set in all complex domains

$$\phi(x, y, 0) = \bar{\phi} + 0.01\text{rand}(x, y), \quad (66)$$

where $\bar{\phi}$ is the average concentration. Here, we consider $\bar{\phi} = 0$ and -0.4 . For all simulations, we use $\Delta t = 0.01$, $h = 1/256$, and $\epsilon = 0.0038$. From top to bottom, the top and middle rows of Fig. 8 show the snapshots of spinodal decomposition in a dumbbell-shaped domain with respect to $\bar{\phi} = 0$ and -0.4 , respectively. When $\bar{\phi} = 0$, two components occupy approximately same proportion and the co-continuous patterns evolve in time. When $\bar{\phi} = -0.4$, the droplet patterns can be observed. The smaller droplets shrink and the bigger droplets grow to form coarser structures. In the nearby regions of irregular boundary, the components contact with the boundary in approximately 90° angles. The last row of Fig. 8 plots the energy curves with respect to different average concentrations. As we can see, the energy dissipation property is satisfied in a dumbbell-shaped domain.

From top to bottom, the top and second rows of Fig. 9 show the spinodal decompositions in a horse-shaped domain with respect to $\bar{\phi} = 0$ and -0.4 . It can be observed that the co-continuous and droplet-shaped patterns appear because of different average concentrations. The energy curves plotted in the last row of Fig. 9 indicate that the energy dissipation property is satisfied in a horse-shaped domain. The corresponding results in a complex domain with T-junctions are displayed in Fig. 10. Although the basic dynamics of CH equation is similar with that in regular domains [6], it can be found that the geometries of irregular domains obviously lead to different distributions of phase patterns.

Next, we consider the phase separation in the irregular domains based on real images. At first, a hand-shaped domain adapted from [50] is used. The initial condition, time step, mesh size, and ϵ are unchanged. The average concentration $\bar{\phi} = 0$ is adopted. The evolutions are shown in the top row of Fig. 11. The next one is a human-shaped domain which is adapted from [51]. Here, the full domain is set to be $\Omega = (0, 0.5) \times (0, 1)$. The mesh size is 128×256 . The snapshots of phase separation in a human-shaped domain are shown in the second row of Fig. 11. We also plot the energy

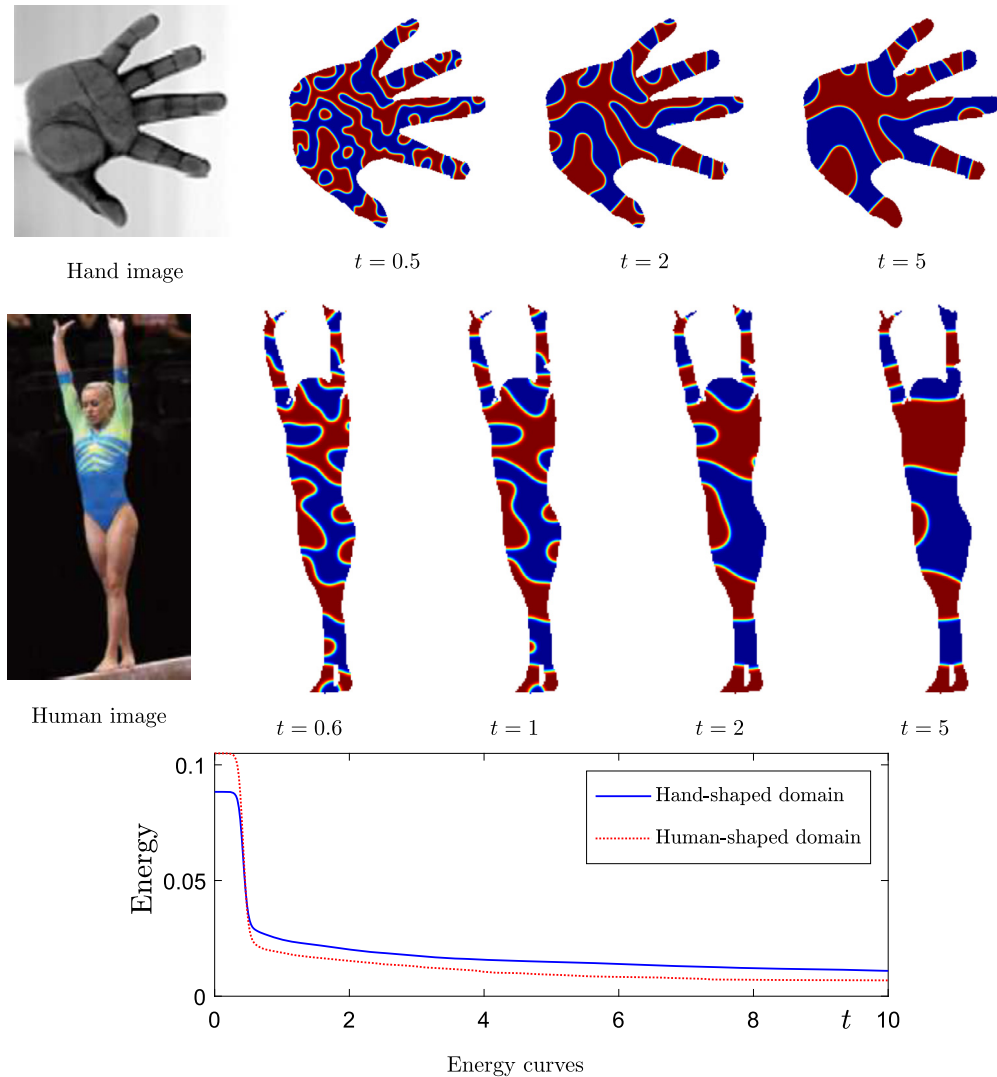


Fig. 11. The top and second rows display the phase separation in a hand-shaped domain and a human-shaped domain. The hand and human images are adapted from [50] and [51]. The last row plots the evolutions of energy.

curves in the last row of Fig. 11. The results in this subsection show that the proposed scheme not only has good capability to simulate spinodal decompositions in various domains but also preserves the energy dissipation property.

3.5. Spinodal decomposition in three-dimensional irregular domains

To further confirm the capability of our proposed method, we investigate the spinodal decompositions in various complex domain in 3D space. The parameters are set to be $\Delta t = 0.01$, $h = 1/128$, $\epsilon = 0.0075$. The initial condition is $\phi(x, y, z, 0) = 0.01\text{rand}(x, y, z)$. As a typical case, the spherical domain with radius $R = 0.45$ is first considered. The top row of Fig. 12 displays the snapshots of phase separation in a spherical domain. Here, the dark blue iso-surface is used to represent the profile of irregular domain. The next simulation is for the spinodal decomposition in the Schoen G domain. The surface of Schoen G is represented by the following function [52]

$$\psi(x, y, z) = \sin(2\pi x) \cos(2\pi y) + \sin(2\pi z) \cos(2\pi x) + \sin(2\pi y) \cos(2\pi z). \quad (67)$$

The evolitional results are shown in the top row of Fig. 13. The last simulation is performed in an alphabet ‘‘H’’ domain [53], its surface is defined as $\psi(x, y, z) = \min(\min(d_1, d_2), d_3)$. Here,

$$\begin{aligned} d_1 &= \min(\max(v_x^1, \max(v_y^1, v_z^1)), 0) + \sqrt{(\max(v_x^1, 0))^2 + (\max(v_y^1, 0))^2 + (\max(v_z^1, 0))^2}, \\ d_2 &= \min(\max(v_x^2, \max(v_y^2, v_z^2)), 0) + \sqrt{(\max(v_x^2, 0))^2 + (\max(v_y^2, 0))^2 + (\max(v_z^2, 0))^2}, \\ d_3 &= \min(\max(v_x^3, \max(v_y^3, v_z^3)), 0) + \sqrt{(\max(v_x^3, 0))^2 + (\max(v_y^3, 0))^2 + (\max(v_z^3, 0))^2}, \end{aligned}$$

where

$$v_x^1 = |x - 0.5 - 2s| - s, \quad v_y^1 = |y - 0.5| - 4s, \quad v_z^1 = |z - 0.5| - 1.5s,$$

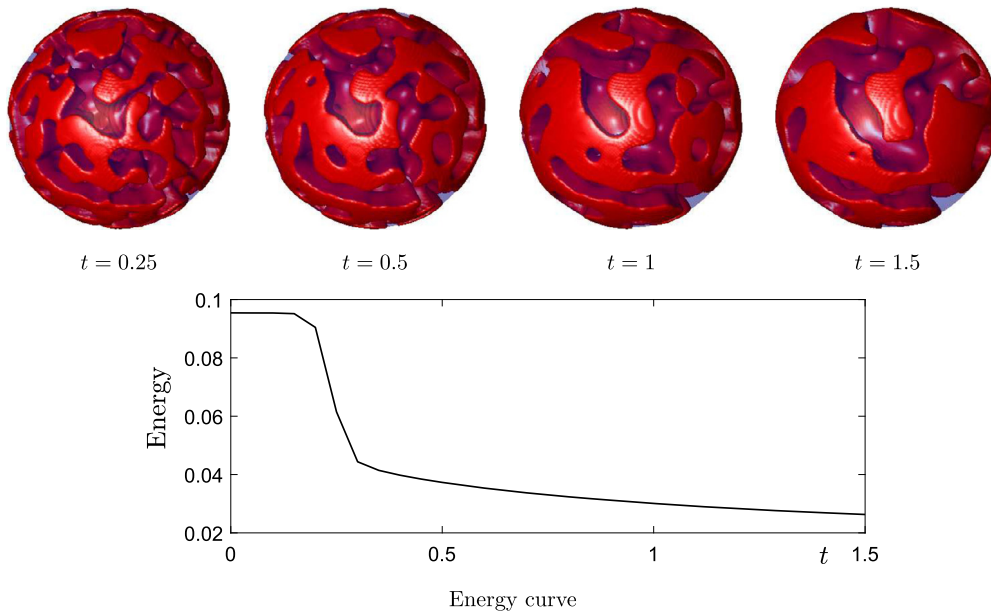


Fig. 12. Spinodal decomposition inside a sphere. The last row plots the energy curve.

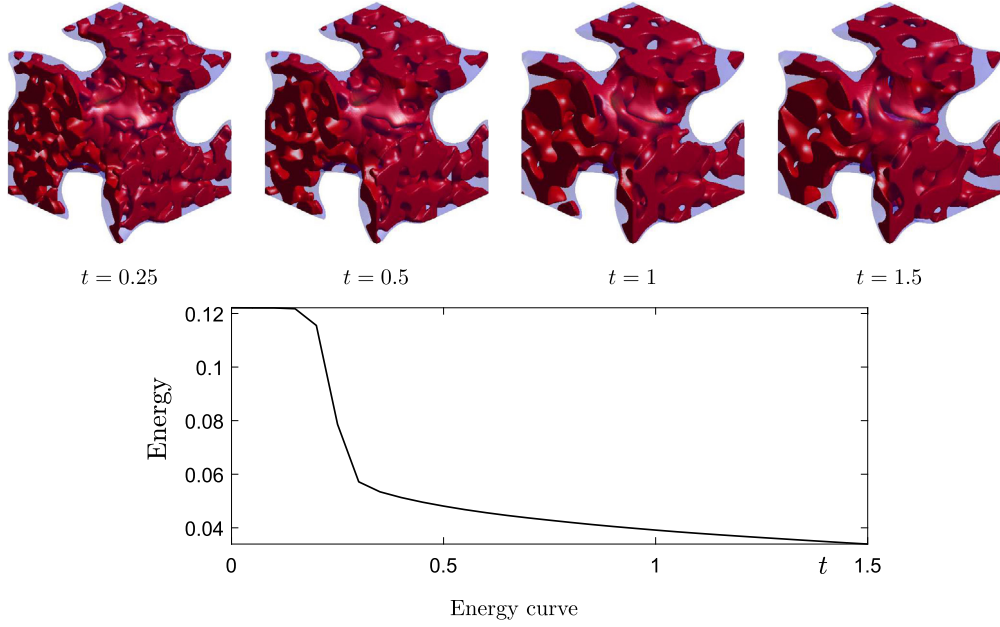


Fig. 13. Spinodal decomposition inside a Schoen G. The last row plots the energy curve.

$$\begin{aligned} v_x^2 &= |x - 0.5 + 2s| - s, & v_y^2 &= |y - 0.5| - 4s, & v_z^2 &= |z - 0.5| - 1.5s, \\ v_x^3 &= |x - 0.5| - 3s, & v_y^3 &= |y - 0.5| - s, & v_z^3 &= |z - 0.5| - 1.5s, \text{ for } s = 0.1. \end{aligned}$$

The evolitional results are shown in the top row of Fig. 14. In the bottom rows of Figs. 12, 13, and 14, the energy curves corresponding to three different 3D domains are plotted. The present computational results demonstrate that the proposed algorithm not only works well in 3D irregular domains but also satisfies the energy dissipation law.

3.6. Phase separation with variable mobilities in complex domains

In previous simulations, we perform the simulations of spinodal decompositions with constant mobility. To show the effect of variable mobility on the evolitional dynamics, we first consider the phase separation in a wavy tube with complex shape [45]. The space-dependent mobility is defined as $M(x) = 0.001 + 0.1x^2/16$. The full domain is set to be $\Omega = (0, 4) \times (0, 1)$. The computational region is bounded by $u(x) = 0.05\sqrt{x}\sin(3\pi x) + 0.75$ and $l(x) = 0.01x^2\cos(2\pi x) - 0.04\sin(6\pi x) + 0.3$. The randomly initial condition with average concentration $\bar{\phi} = 0$ is used. We set $\Delta t = 0.01$, $h = 1/128$, and $\epsilon = 0.0075$. The left and right columns of Fig. 15 show the snapshots of phase separation with respect to a space-dependent mobility $M(x)$ and a constant mobility $M = 0.1$, respectively. When a constant mobility is used, we observe that the evolitional speed at each spatial point is same. On the contrary, the space-dependent mobility obviously suppresses the dynamics along the left side of complex domain.

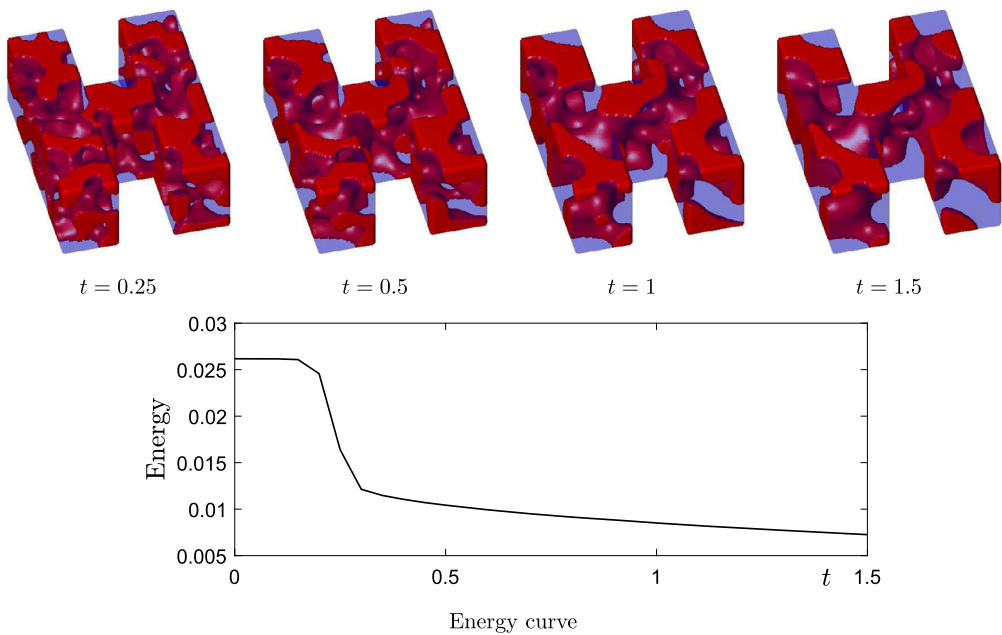


Fig. 14. Spinodal decomposition inside an alphabet “H”. The last row plots the energy curve.

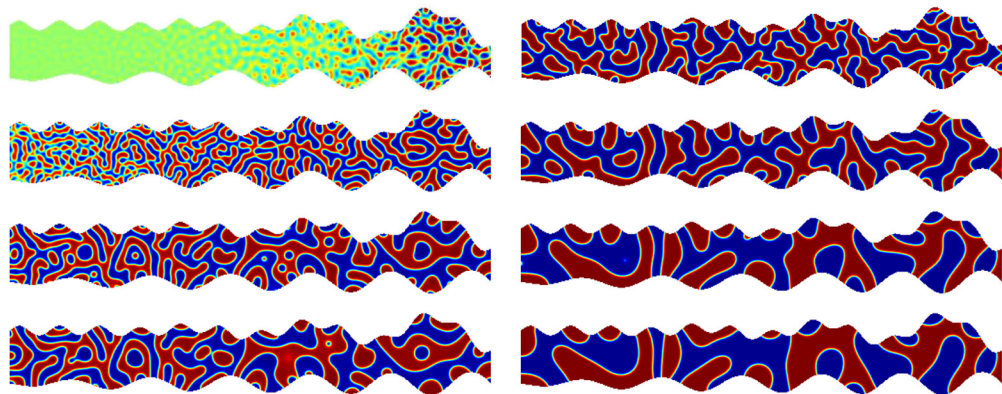


Fig. 15. Phase separation in a wavy tube with respect to a space-dependent mobility (left) and a constant mobility (right). From top to bottom, the results are at $t = 0.4, 1, 3$, and 5 .

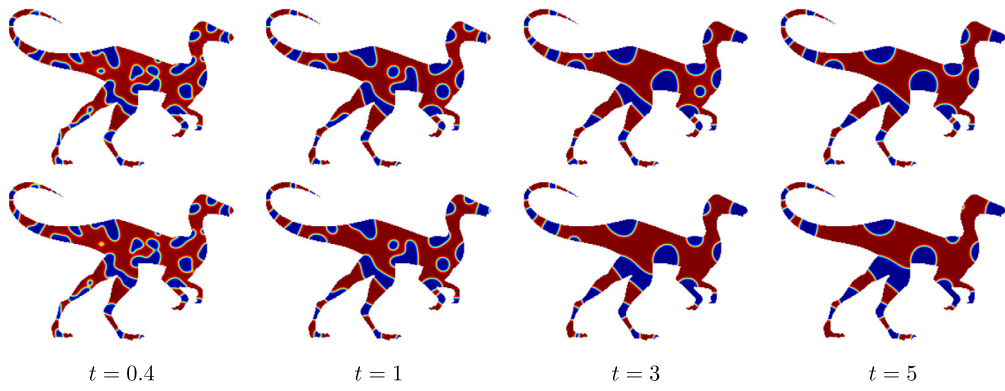


Fig. 16. Phase separation in a velociraptor-shaped domain. The top and bottom rows correspond to $M(\phi) = 0.1|1 - \phi^2|$ and $M = 0.1$, respectively.

Although there have been numerous simulations on the CH equation with constant mobility, it should be noted that the CH model was originally derived with a degenerate mobility. In this work, we consider a typical degenerate mobility as $M(\phi) = 0.1|1 - \phi^2|$. This form significantly lowers the long-range diffusion across bulk phases. The average concentration $\bar{\phi} = 0.3$ is used. The top row of Fig. 16 displays the snapshots of phase separation in a velociraptor-shaped domain with respect to a degenerate mobility. The bottom row of Fig. 16 displays the computational results with respect to a constant mobility, i.e., $M = 0.1$. It can be observed that the degenerate mobility lowers the shrinkage rate of those smaller droplets because the long-range diffusion in bulk regions is weakened.

4. Conclusions

To accurately and efficiently simulate the two-phase spinodal decomposition in arbitrarily irregular domains, a SSP-IMEX RK approach was used to design the linear numerical schemes in time. The temporally first-order accuracy and second-order accuracy were achieved by using two-step and three-step strategies. The FDM was considered to discretize the space. An appropriate boundary control function was introduced to transform the original equations into equivalent forms in complex domains. Because of the property of boundary control functional, the discrete versions of mass conservation and unconditional energy dissipation law could be strictly proved. In each time iteration, the solution could be efficiently updated by solving several linear elliptic type equations and the conservative multigrid algorithm was also presented to accelerate the convergence. The energy dissipation property, mass conservation, and convergence rates with respect to time and space were confirmed by the numerical experiments. The simulations in 2D irregular domains (i.e., circle, dumbbell, micro-fluid device, horse, human, and hand) and 3D irregular domains (i.e., sphere, Schoen G, and alphabet H) showed that the proposed method had desired capability. In upcoming works, we will extend the present idea to develop efficient and energy-stable methods for the L^2 -gradient flows [54,55], the N -component ($N \geq 3$) phase-field models [9,56–59], the phase-field dendritic growth model [60], and the incompressible fluid flows coupled phase-field systems [61–63] in arbitrarily complex domains.

Data availability

Data will be made available on request.

Acknowledgement

J. Yang is supported by the National Natural Science Foundation of China (No. 12201657), the China Postdoctoral Science Foundation (No. 2022M713639), and the 2022 International Postdoctoral Exchange Fellowship Program (Talent-Introduction Program) (No. YJ20220221). The author (J.S. Kim) was supported by the National Research Foundation of Korea (NRF) grant funded by the Korea government (MSIT) (No. 2022R1A2C1003844). The work of Z. Tan is supported by the National Nature Science Foundation of China (11971502), Guangdong Natural Science Foundation (2022A1515010426), Guangdong Province Key Laboratory of Computational Science at the Sun Yat-sen University (2020B1212060032), and Key-Area Research and Development Program of Guangdong Province (2021B0101190003). The authors thank the anonymous reviewers for constructive comments on the revision.

References

- [1] M. Sun, X. Xiao, X. Feng, K. Wang, Modeling and numerical simulation of surfactant systems with incompressible fluid flows on surfaces, *Comput. Methods Appl. Mech. Eng.* 390 (2022) 114450.
- [2] B. Xia, C. Mei, Q. Yu, Y. Li, A second order unconditionally stable scheme for the modified phase field crystal model with elastic interaction and stochastic noise effect, *Comput. Methods Appl. Mech. Eng.* 363 (2020) 112795.
- [3] S. Aihara, T. Takaki, N. Takada, Multi-phase-field modeling using a conservative Allen–Cahn equation for multiphase flow, *Comput. Fluids* 178 (2019) 141–151.
- [4] J.W. Cahn, J.E. Hilliard, Free energy of a non-uniform system I: interfacial free energy, *J. Chem. Phys.* 28 (1958) 258–267.
- [5] D. Lee, J.Y. Huh, D. Jeong, J.M. Shin, A. Yun, J. Kim, Physical, mathematical, and numerical derivations for the Cahn–Hilliard equations, *Comput. Mater. Sci.* 81 (2014) 216–225.
- [6] J. Kim, S. Lee, Y. Choi, S.M. Lee, D. Jeong, Basic principles and practical applications of the Cahn–Hilliard equation, *Math. Probl. Eng.* 2016 (2016) 9532608.
- [7] J. Yang, J. Kim, An energy stable second-order accurate scheme for microphase separation of periodic diblock copolymers, *East Asian J. Appl. Math.* 11 (2) (2021) 234–254.
- [8] Y. Li, J. Kim, N. Wang, An unconditionally energy-stable second-order time-accurate scheme for the Cahn–Hilliard equation on surfaces, *Commun. Nonlinear Sci. Numer. Simul.* 53 (2017) 213–227.
- [9] J. Yang, J. Kim, An unconditionally stable second-order accurate method for systems of Cahn–Hilliard equations, *Commun. Nonlinear Sci. Numer. Simul.* 87 (2020) 105276.
- [10] H.G. Lee, A non-iterative and unconditionally energy stable method for the Swift–Hohenberg equation with quadratic-cubic nonlinearity, *Appl. Math. Lett.* 123 (2022) 107579.
- [11] F. Zhang, D. Li, H.W. Sun, J.L. Zhang, A stabilized fully-discrete scheme for phase field crystal equation, *Appl. Numer. Math.* 178 (2022) 337–355.
- [12] S. Lee, J. Shin, Energy stable compact scheme for Cahn–Hilliard equation with periodic boundary condition, *Comput. Math. Appl.* 77 (1) (2019) 189–198.
- [13] Y. Li, D. Jeong, H. Kim, C. Lee, J. Kim, Comparison study on the different dynamics between the Allen–Cahn and the Cahn–Hilliard equations, *Comput. Math. Appl.* 77 (2019) 311–322.
- [14] H. Liang, Y. Li, J. Chen, J. Xu, Axisymmetric lattice Boltzmann model for multiphase flows with large density ratio, *Int. J. Heat Mass Transf.* 130 (2019) 1189–1205.
- [15] C. Zhang, Z. Guo, H. Liang, High-order lattice-Boltzmann model for the Cahn–Hilliard equation, *Phys. Rev. E* 99 (2019) 043310.
- [16] H. Liang, C. Zhang, R. Du, Y. Wei, Lattice Boltzmann method for fractional Cahn–Hilliard equation, *Commun. Nonlinear Sci. Numer. Simul.* 91 (2020) 105443.
- [17] D.J. Eyre, Unconditionally gradient stable time marching the Cahn–Hilliard equation, in: J.W. Bullard, L.-Q. Chen (Eds.), *Computational and Mathematical Models of Microstructural Evolution*, in: MRS Proceedings, vol. 529, Cambridge University Press, Cambridge, 1998, pp. 39–46.
- [18] Y. Yan, W. Chen, C. Wang, S. Wise, A second-order energy stable BDF numerical scheme for the Cahn–Hilliard equation, *Commun. Comput. Phys.* 23 (2018) 576–602.
- [19] K. Cheng, W. Feng, C. Wang, S. Wise, An energy stable fourth order finite difference scheme for the Cahn–Hilliard equation, *J. Comput. Appl. Math.* 362 (2019) 574–595.
- [20] W. Chen, C. Wang, X. Wang, S. Wise, Positivity-preserving, energy stable numerical schemes for the Cahn–Hilliard equation with logarithmic potential, *J. Comput. Phys. X* 3 (2019) 100031.
- [21] W. Chen, W. Feng, Y. Liu, C. Wang, S. Wise, A second order energy stable scheme for the Cahn–Hilliard–Hele–Shaw equation, *Discrete Contin. Dyn. Syst., Ser. B* 24 (2019) 149–182.
- [22] A. Diegel, C. Wang, X. Wang, S. Wise, Convergence analysis and error estimates for a second order accurate finite element method for the Cahn–Hilliard–Navier–Stokes system, *Numer. Math.* 135 (2017) 495–534.
- [23] Y. Qin, C. Wang, Z. Zhang, A positivity-preserving and convergent numerical scheme for the binary fluid-surfactant system, *Int. J. Numer. Anal. Model.* 18 (3) (2021) 399–425.
- [24] J. Guo, C. Wang, S. Wise, X. Yue, An H^2 convergence of a second-order convex-splitting, finite difference scheme for the three-dimensional Cahn–Hilliard equation, *Commun. Math. Sci.* 14 (2016) 489–515.
- [25] A. Diegel, C. Wang, S. Wise, Stability and convergence of a second order mixed finite element method for the Cahn–Hilliard equation, *IMA J. Numer. Anal.* 36 (2016) 1867–1897.
- [26] K. Cheng, C. Wang, S. Wise, X. Yue, A second-order, weakly energy-stable pseudo-spectral scheme for the Cahn–Hilliard equation and its solution by the homogeneous linear iteration method, *J. Sci. Comput.* 69 (2016) 1083–1114.
- [27] J. Guo, C. Wang, S. Wise, X. Yue, An improved error analysis for a second-order numerical scheme for the Cahn–Hilliard equation, *J. Comput. Appl. Math.* 388 (2021) 113300.
- [28] H.G. Lee, An energy stable method for the Swift–Hohenberg equation with quadratic-cubic nonlinearity, *Comput. Methods Appl. Mech. Eng.* 343 (2019) 40–51.
- [29] J. Shin, H.G. Lee, J.-Y. Lee, Convex splitting Runge–Kutta methods for phase-field models, *Comput. Math. Appl.* 73 (2017) 2388–2403.
- [30] J. Shin, H.G. Lee, J.-Y. Lee, Long-time simulation of the phase-field crystal equation using high-order energy-stable CSRK methods, *Comput. Methods Appl. Mech. Eng.* 364 (6) (2020) 112981.
- [31] H. Song, Energy SSP-IMEX Runge–Kutta methods for the Cahn–Hilliard equation, *J. Comput. Appl. Math.* 292 (2016) 576–590.
- [32] Y. Li, R. Liu, Q. Xia, C. He, Z. Li, First- and second-order unconditionally stable direct discretization methods for multi-component Cahn–Hilliard system on surfaces, *J. Comput. Appl. Math.* 401 (2022) 113778.
- [33] J. Kou, S. Sun, X. Wang, A novel energy factorization approach for the diffuse-interface model with Peng–Robinson equation of state, *SIAM J. Sci. Comput.* 42 (2020) B30–B56.

- [34] X. Wang, J. Kou, H. Gao, Linear energy stable and maximum principle preserving semi-implicit scheme for Allen–Cahn equation with double well potential, *Commun. Nonlinear Sci. Numer. Simul.* 98 (2021) 105766.
- [35] F. Guillén-González, G. Tierra, On linear schemes for the Cahn–Hilliard diffuse interface model, *J. Comput. Phys.* 234 (2013) 140–171.
- [36] S. Pei, Y. Hou, Q. Li, A linearly second-order, unconditionally energy stable scheme and its error estimates for the modified phase field crystal equation, *Comput. Math. Appl.* 103 (2021) 104–126.
- [37] G. Zhu, J. Kou, B. Yao, Y.S. Wu, J. Yao, S. Sun, Thermodynamically consistent modelling of two-phase flows with moving contact line and soluble surfactants, *J. Fluid Mech.* 879 (2019) 327–359.
- [38] J. Zhao, A general framework to derive linear, decoupled and energy-stable schemes for reversible-irreversible thermodynamically consistent models, *Comput. Math. Appl.* 110 (2022) 91–109.
- [39] G. Zhu, H. Chen, J. Yao, S. Sun, Efficient energy-stable schemes for the hydrodynamics coupled phase-field model, *Appl. Math. Model.* 70 (2019) 82–108.
- [40] Y. Li, J.I. Choi, J. Kim, Multi-component Cahn–Hilliard system with different boundary conditions in complex domains, *J. Comput. Phys.* 323 (2016) 1–16.
- [41] D. Jeong, J. Yang, J. Kim, A practical and efficient numerical method for the Cahn–Hilliard equation in complex domains, *Commun. Nonlinear Sci. Numer. Simul.* 73 (2019) 217–228.
- [42] Z. Guo, F. Yu, P. Lin, S. Wise, J. Lowengrub, A diffuse domain method for two-phase flows with large density ratio in complex geometries, *J. Fluid Mech.* 907 (2021) A38.
- [43] H.R. Liu, P. Gao, H. Ding, Fluid-structure interaction involving dynamic wetting: 2D modeling and simulations, *J. Comput. Phys.* 348 (2017) 45–65.
- [44] H.L. Li, H.R. Liu, H. Ding, A fully 3D simulation of fluid-structure interaction with dynamic wetting and contact angle hysteresis, *J. Comput. Phys.* 420 (2020) 109709.
- [45] J. Shin, D. Jeong, J. Kim, A conservative numerical method for the Cahn–Hilliard equation in complex domains, *J. Comput. Phys.* 230 (2011) 7441–7455.
- [46] H.G. Lee, Stability condition of the second-order SSP-IMEX-RK method for the Cahn–Hilliard equation, *Mathematics* 8 (1) (2020) 11.
- [47] J. Kim, K. Kang, J. Lowengrub, Conservative multigrid methods for Cahn–Hilliard fluids, *J. Comput. Phys.* 193 (2) (2004) 511–543.
- [48] Z. Fu, T. Tang, J. Yang, Energy plus maximum bound preserving Runge–Kutta methods for the Allen–Cahn equation, *J. Sci. Comput.* 92 (2022) 97.
- [49] D.R. Link, S.L. Anna, D.A. Weitz, H.A. Stone, Geometrically mediated breakup of drops in microfluidic devices, *Phys. Rev. Lett.* 92 (2004) 054503.
- [50] D. Jeong, S. Kim, C. Lee, J. Kim, An accurate and practical explicit hybrid method for the Chan–Vese image segmentation model, *Mathematics* 8 (2020) 1173.
- [51] Y. Li, S. Yoon, J. Wang, J. Park, S. Kim, C. Lee, H. Kim, J. Kim, Fast and efficient numerical finite difference method for multiphase image segmentation, *Math. Probl. Eng.* 2021 (2021) 2414209.
- [52] S.D. Yang, H.G. Lee, J. Kim, A phase-field approach for surface area minimization of triply-periodic surfaces with volume constraint, *Comput. Phys. Commun.* 181 (2010) 1037–1046.
- [53] D. Jeong, Y. Li, C. Lee, J. Yang, J. Kim, A conservative numerical method for the Cahn–Hilliard equation with generalized mobilities on curved surfaces in three-dimensional space, *Commun. Comput. Phys.* 27 (2) (2020) 412–430.
- [54] H.G. Lee, J. Shin, J-Y. Lee, A high-order and unconditionally energy stable scheme for the conservative Allen–Cahn equation with a nonlocal Lagrange multiplier, *J. Sci. Comput.* 90 (2022) 51.
- [55] Q. Li, L. Mei, Numerical approximation of the two-component PFC models for binary colloidal crystals: efficient, decoupled, and second-order unconditionally energy stable schemes, *J. Sci. Comput.* 88 (2021) 60.
- [56] R. Haghani-Hassan-Abadi, A. Fakhari, M.H. Rahimian, Numerical simulation of three-component multiphase flows at high density and viscosity ratios using lattice Boltzmann methods, *Phys. Rev. E* 97 (2018) 033312.
- [57] J. Yang, J. Kim, Numerical study of the ternary Cahn–Hilliard fluids by using an efficient modified scalar auxiliary variable approach, *Commun. Nonlinear Sci. Numer. Simul.* 102 (2021) 105923.
- [58] W. Chen, C. Wang, S. Wang, X. Wang, S.M. Wise, Energy stable numerical schemes for ternary Cahn–Hilliard system, *J. Sci. Comput.* 84 (2020) 27.
- [59] L. Dong, C. Wang, S.M. Wise, Z. Zhang, A positivity-preserving, energy stable scheme for a ternary Cahn–Hilliard system with the singular interfacial parameters, *J. Comput. Phys.* 442 (2021) 110451.
- [60] M. Ohno, T. Takaki, Y. Shibuta, Numerical testing of quantitative phase-field models with different polynomials for isothermal solidification in binary alloys, *J. Comput. Phys.* 335 (2017) 621–636.
- [61] Q. Xia, Q. Yu, Y. Li, A second-order accurate, unconditionally energy-stable numerical scheme for binary fluid flows on arbitrarily curved surfaces, *Comput. Methods Appl. Mech. Eng.* 384 (2021) 113987.
- [62] Q. Xia, J. Kim, B. Xia, Y. Li, An unconditionally energy stable method for binary incompressible heat conductive fluids based on the phase-field model, *Comput. Math. Appl.* 123 (2022) 26–39.
- [63] X. Pan, S. Chun, J-I. Choi, Efficient monolithic projection-based method for chemotaxis-driven bioconvection problems, *Comput. Math. Appl.* 84 (2021) 166–184.